

Three-flavor atmospheric neutrino anomaly

G. L. Fogli^b, E. Lisi^{a,b}, D. Montanino^b, and G. Scioscia^b

^a*Institute for Advanced Study, Princeton, New Jersey 08540*

^b*Dipartimento di Fisica dell'Università and Sezione INFN di Bari, 70126 Bari, Italy*

Abstract

We investigate the indications of flavor oscillations that come from the anomalous flavor composition of the atmospheric neutrino flux observed in some underground experiments. We study the information coming from the neutrino-induced μ -like and e -like events both in the sub-GeV energy range (Kamiokande, IMB, Fréjus, and NUSEX experiments) and in the multi-GeV energy range (Kamiokande experiment). First we analyze all the data in the limits of pure $\nu_\mu \leftrightarrow \nu_\tau$ and $\nu_\mu \leftrightarrow \nu_e$ oscillations. We obtain that $\nu_\mu \leftrightarrow \nu_e$ oscillations provide a better fit, in particular to the multi-GeV data. Then we perform a three-flavor analysis in the hypothesis of dominance of one neutrino square mass difference, m^2 , implying that the neutrino mixing is parametrized by two angles, $(\psi, \phi) \in [0, \pi/2]$. We explore the space (m^2, ψ, ϕ) exhaustively, and find the regions favored by the oscillation hypothesis. The results are displayed in a form suited to the comparison with other flavor oscillation searches at accelerator, reactor, and solar ν experiments. In the analysis, we pay particular attention to the earth matter effects, to the correlation of the uncertainties, and to the symmetry properties of the oscillation probability.

PACS number(s): 14.60.Pq, 95.85.Ry, 13.15.+g

I. INTRODUCTION

The indication for an anomalous muon and electron flavor composition of the observed atmospheric neutrino flux represents a still unsolved puzzle (for recent reviews, see [1]). A possible explanation could be provided by neutrino flavor oscillations. In this paper we adopt such a viewpoint and explore systematically its consequences in a three-flavor framework with one dominant neutrino square mass difference.

We perform a comprehensive and accurate analysis of the experimental information coming from the Kamiokande [2–4], IMB [5,6], Frejus [7,8], and NUSEX [9] atmospheric neutrino experiments. We do not characterize the atmospheric neutrino anomaly with the popular double flavor ratio $R_{\mu/e} = (\mu/e)_{\text{data}}/(\mu/e)_{\text{theory}}$ which, as discussed in [10], is affected by non-Gaussian uncertainties. Instead we separate the μ -like and e -like event rates, whose errors are normally distributed [10]. We compare the data with the theoretical expectations in the presence of two-flavor and three-flavor oscillations, including the earth matter effects [11,12]. We place significant bounds in the oscillation parameter space, which can provide useful guidelines for model building, for the expectations at the running SuperKamiokande experiment [13], and for the discovery potential at future long-baseline neutrino oscillation experiments [14]. We also highlight the interplay between the results of this work and those obtained—within the same theoretical framework—from the analysis of flavor oscillation searches in accelerator and reactor [15] or solar [16] neutrino experiments. We include a larger data set and use a more refined statistical approach than previous three-flavor analyses of the atmospheric neutrino anomaly performed by other authors [17–27] and by ourselves [15,28,29].

The paper has the following structure. In Sec. II we introduce the experimental ingredients of the analysis and describe their treatment. In Sec. III we briefly recall the properties of three-flavor oscillations in the hypothesis of one dominant square mass difference. In Sec. IV we perform the data analysis in the subcases of two-flavor $\nu_\mu \leftrightarrow \nu_\tau$ and $\nu_\mu \leftrightarrow \nu_e$ oscillations. In Sec. V we present the main results of our analysis of three-flavor atmospheric neutrino oscillations and discuss their relation with the indications coming from other (laboratory and solar) neutrino oscillation experiments. In Sec. VI we summarize our work and draw our conclusions. In Appendices A, B, and C, we discuss respectively our treatment of the Kamiokande multi-GeV neutrino data, the correlation of the theoretical uncertainties, and the symmetry properties of the neutrino oscillation probability.

II. EXPERIMENTAL INGREDIENTS AND THEIR ANALYSIS

In this section we introduce the experimental data and discuss briefly some technical aspects of their analysis.

A. Experimental data

We analyze the largest set of data on the electron and muon composition of the atmospheric neutrino flux, which can be considered both homogeneous and statistically consistent. In particular, we include the neutrino-induced e -like and μ -like event rates measured by the

four experiments Kamiokande [2,3], IMB [5,6], Fréjus [7,8], and NUSEX [9] at low energies (so-called sub-GeV data), and by the Kamiokande experiment at higher energies in five zenith-angle sectors [4] (so-called multi-GeV data).¹ Concerning the multi-GeV data, we will consider either the information coming from the binned angular distribution of events (“binned multi-GeV”), or the reduced information coming from the angle-integrated number of events (“unbinned multi-GeV”).

As it is well known, the Fréjus and NUSEX measurements do not confirm the Kamiokande and IMB observation of an anomalous muon-electron flavor composition of the atmospheric events [30]. However, all the data are statistically compatible within $\sim 2\sigma$ or better (see Fig. 3 in [10]) and their combination in a global analysis is reasonable.

We do not include the higher-energy data pertaining only to the muon flavor content, the so-called upward-going muons (see, e.g., [31]). This data set has specific experimental characteristics and deserves a separate theoretical analysis (in progress). However, we will briefly comment on upward-going muons in due course.² We also do not include the data from the Soudan 2 experiment [33], because a detailed, official analysis has not been published yet by the experimental collaboration.

We emphasize that, according to the discussion in [10], we prefer to separate the electron and muon flavor information, instead of using the popular ratio $R_{\mu/e} = (\mu/e)_{\text{data}}/(\mu/e)_{\text{theory}}$. The ratio $R_{\mu/e}$ allows a large cancellation of the theoretical errors [30], but its probability distribution is highly non-Gaussian.³ We have shown [10] that one can use only normally distributed variables provided that, when the μ and e experimental and theoretical rates are separated, the correlations of their uncertainties are included.

In the comparison of the data with theoretical predictions, we use a χ^2 statistic including both experimental and theoretical uncertainties, with the proper error correlation matrix [10].

B. Neutrino fluxes and interactions

In order to get significant constraints on the neutrino oscillation hypothesis, the measured numbers of μ -like and e -like events produced by neutrinos and antineutrinos in each detector must be compared with detailed theoretical predictions.

The theoretical calculations involve the numerical estimate of integrals of the kind:

$$I_{\alpha\beta} = \int d\theta \int dE_\nu \frac{d^2\Phi_\alpha}{dE_\nu d\theta} P_{\alpha\beta} \int dE_\ell \frac{d\sigma_\beta}{dE_\ell} \varepsilon_\beta , \quad (1)$$

¹ We always include both fully and partially contained events in the multi-GeV Kamiokande data sample.

² We note in passing that the recent reanalysis of the data from the Fréjus experiment [32] is relevant for the high-energy muon fluxes, but it does not change significantly the previous Fréjus results [7,8] on low-energy e -like and μ -like events.

³ The ratio of two normally distributed variables obeys a Cauchy distribution.

where θ is the zenith angle, α and β are flavor indices, E_ν and E_ℓ are the (anti)neutrino and lepton energies, Φ is the atmospheric (anti)neutrino flux, P is the oscillation probability, σ is the (anti)neutrino interaction cross-section, and ε is the lepton detection efficiency. Our estimate of the $I_{\alpha\beta}$'s in the multi-GeV energy range is discussed in Appendix A.

Concerning the sub-GeV experiments, the ingredients Φ , σ , and ε that we use to compute the $I_{\alpha\beta}$'s have been reported in our previous works [28,29]. In particular, we use the Bartol group calculations of Φ [34,35] for the electron and muon neutrino and antineutrino fluxes at each detector location.

The Bartol fluxes [34] have been used by all the four sub-GeV experiments in at least one simulation, and thus provide us with the advantages of a uniform data analysis and of a homogeneous comparison of our calculations with the published detector simulations. This comparison has been done in [28,29]. In particular, we refer the reader to Fig. 1 in [29], where our absolute predictions for the lepton energy spectra are superposed to the corresponding published Monte Carlo simulations of the Kamiokande, IMB, Fréjus, and NUSEX experiments (in absence of oscillations). The agreement of our calculations with the published spectra is good.

Since this work was initiated, new refined atmospheric neutrino flux calculations have appeared [36,37]. These new fluxes, as far as we know from the published literature, have not been used yet by the experimental collaborations to reprocess their simulations or to reanalyze their data, and are not used in this work either. However, in the statistical analysis we conservatively associate a $\pm 30\%$ uncertainty (1σ) with the absolute theoretical neutrino fluxes. This error accounts conservatively for the spread in the atmospheric neutrino calculations published so far [10]. The uncertainties of the μ and e neutrino fluxes are highly correlated (see [10] and Appendix B for more details). Such correlation is even more important than the absolute magnitude of the errors themselves in driving the fits to atmospheric ν data. In fact, it will be shown that a reduction of the flux error from our default value, $\sigma_{\text{flux}} = 30\%$, to $\sigma_{\text{flux}} = 20\%$ or even 15% does not change significantly the results of the oscillation fits. In the absence of oscillations, it has already been shown in Ref. [10] (Table III) that the statistical significance of the anomaly does not change much by reducing the flux error from 30% to 20% .

The last ingredient of Eq. (1) to be discussed is the oscillation probability $P_{\alpha\beta}$. This is the subject of the next Section.

III. THEORETICAL FRAMEWORK

The calculation of the atmospheric neutrino oscillation probabilities requires a well-defined theoretical framework. The three-flavor framework used in this paper is completely specified by the neutrino spectrum shown in Fig. 1.

In Fig. 1 we show the adopted spectrum of neutrino mass eigenstates (ν_1, ν_2, ν_3). Two states (ν_1, ν_2) are assumed to be almost degenerate in mass. The third state, ν_3 , is largely separated in mass from the almost degenerate doublet, with $|m_3^2 - m_{1,2}^2| \simeq m^2$ being the dominant square mass difference driving the atmospheric neutrino oscillations. This situation can be realized either in scenario (a) or in scenario (b) of Fig. 1, that is, with ν_3 either lighter or heavier than ν_1 and ν_2 .

In both scenarios of Fig. 1, the subdominant square mass difference between ν_2 and ν_1 , $\delta m^2 = m_2^2 - m_1^2$, is assumed to be too small to produce detectable effects in the energy range explored by current atmospheric neutrino experiments. This assumption holds, for instance, if the parameter δm^2 is used to fit solar neutrino data [16] ($\delta m^2 \simeq 5 \times 10^{-6} \text{ eV}^2$ at the best-fit point for matter-enhanced oscillations). At the scale of the atmospheric neutrino experiments, we simply set $\delta m^2 = 0$. The limits of this approximation are commented in Sec. V C. The same approximation has been used in [15] where we studied accelerator and reactor neutrino oscillations, and to which we refer the reader for further details and references. We collectively consider the accelerator, reactor, and atmospheric neutrino experiments as “terrestrial” oscillation experiments.

At zeroth order in $\delta m^2/m^2$ the two scenarios of Fig. 1 are physically different for atmospheric neutrinos propagating in the earth matter (see Appendix C), while they are not distinguishable either by means of accelerator and reactor neutrino oscillation searches (in vacuum) [15] or by solar neutrino oscillations (in vacuum or in matter) [16]. In this sense, atmospheric neutrinos potentially provide a unique information on the neutrino spectrum.

Notice that the spectra (a) and (b) in Fig. 1 are simply related by:

$$(a) \rightarrow (b) \iff +m^2 \rightarrow -m^2 . \quad (2)$$

In the following, we will explicitly distinguish cases (a) and (b) whenever necessary.

In the framework characterized by the spectrum of Fig. 1 one has two important simplifications with respect to the most general three-flavor oscillation scenario (see [15] and Appendix C): (1) neutrino mixing in terrestrial oscillation experiments can be described by just two mixing angles, ψ and ϕ ; and (2) effects related to the a possible CP violating phase are unobservable. It follows that the parameter space for terrestrial (including atmospheric) three-flavor neutrino oscillations can be described in terms of three parameters: (m^2, ψ, ϕ) .

The angles ψ and ϕ are defined as in [38]. In the standard parametrization of the mixing matrix [39] the following identifications hold:

$$\psi = \theta_{23}, \quad \phi = \theta_{13} . \quad (3)$$

The three-flavor framework with one dominant square mass difference is the simplest extension of the two-generation formalism in which all the two-flavor oscillation channels are open. The subcases of pure two-flavor oscillations $\nu_e \leftrightarrow \nu_\tau$, $\nu_\mu \leftrightarrow \nu_e$, and $\nu_\mu \leftrightarrow \nu_\tau$, are recovered in the limits $\psi = 0$, $\psi = \pi/2$, and $\phi = 0$ respectively. A clear graphical representation of the general three-flavor case and of its two-flavor limits is provided by Fig. 2 in [15]. Here we do not pay attention to the $\nu_e \leftrightarrow \nu_\tau$ subcase, since it does not solve—but rather aggravates—the atmospheric neutrino anomaly. We will briefly comment on a theoretically interesting, genuine three-flavor subcase of this framework, the so-called threefold maximal mixing scenario [40,41], in Sec. V. In our notation, threefold maximal mixing corresponds to $(\tan^2 \psi, \tan^2 \phi) = (1, 1/2)$ at any m^2 .

With a neutrino mass spectrum as in Fig. 1, the calculation of the vacuum oscillation probability for neutrinos arriving from above the horizon is straightforward (see Appendix C). However, the vacuum approximation is not adequate for neutrinos which travel in the earth matter for a large fraction of their path length. For these neutrinos one expects substantial deviations from the vacuum oscillation probability [42–46,23] when

$m^2 \sim 2\sqrt{2}G_F\bar{N}_e E_\nu$, where \bar{N}_e is the typical electron density along the neutrino trajectory. This implies significant matter effects in the range $m^2 \sim 10^{-4}$ – 10^{-3} eV² for sub-GeV observables and in the range $m^2 \sim 10^{-3}$ – 10^{-2} eV² for multi-GeV observables.⁴ Moreover, a genuine three-flavor effect takes place [23]: the effective mass eigenstates $\nu'_{1,2}$ in matter are not exactly degenerate, and the phase variation associated to their splitting is relevant for path lengths comparable to the earth radius. This additional phase disappears in the two-flavor subcases, since one of the “degenerate” neutrinos decouples.

We take into account the earth matter effects by solving numerically the neutrino propagation equations with an assigned earth density profile [47]. In order to save computer time, the density profile is modeled as a 5-step function [29] with steps corresponding to the five relevant radial shells. This approximation is sufficiently accurate for our purposes.

We have a final remark on the graphical representations of the results. In [15] we have shown that the three-flavor parameter space for terrestrial neutrino oscillations can be usefully charted using the (logarithmic) coordinates $(m^2, \tan^2 \psi, \tan^2 \phi)$. In the following, the results of our analysis will be displayed in several plane sections of the space $(m^2, \tan^2 \psi, \tan^2 \phi)$ at fixed values of either m^2 , ϕ , or ψ .

IV. TWO-FLAVOR ANALYSIS

In this section we show the results of our analysis in the subcases of pure $\nu_\mu \leftrightarrow \nu_\tau$ and $\nu_\mu \leftrightarrow \nu_e$ two-flavor oscillations. The discussion of these cases is interesting in itself, and helps in understanding the more complicated situation of three-flavor oscillations.

A. Pure $\nu_\mu \leftrightarrow \nu_\tau$ oscillations

In our framework we recall that the subcase of pure $\nu_\mu \leftrightarrow \nu_\tau$ oscillations is reached in the limit $\phi \rightarrow 0$, which leaves (m^2, ψ) as relevant variables. This subcase is particularly simple from a theoretical viewpoint, since ν_e is decoupled and thus the earth matter does not affect the oscillations. As a consequence (see Appendix C), the scenarios (a) and (b) in Fig. 1 become physically equivalent, and the formalism is invariant under the substitution $\psi \rightarrow \frac{\pi}{2} - \psi$. One usually takes advantage of this symmetry to restrict the range of the mixing angle ψ to $[0, \pi/4]$. Here we show the full range $\psi \in [0, \pi/2]$ in order to mark the difference with the $\nu_\mu \leftrightarrow \nu_e$ case (Sec. IV B), where the symmetry $\psi \rightarrow \frac{\pi}{2} - \psi$ is broken by matter effects.

In Fig. 2 we show the results of our analysis as bounds in the $(\tan^2 \psi, m^2)$ plane at 90% C.L. (solid lines) and 99% C.L. (dotted lines), which corresponds to $\Delta\chi^2 = 4.61$ and 9.21 respectively ($N_{\text{DF}} = 2$). Notice the mirror symmetry of all the curves with respect to the axis $\psi = \pi/4$.

⁴ It should be noted, however, that matter effects do not totally disappear even in the limit $m^2 \rightarrow \infty$, see Appendix C.

To avoid ambiguities, the allowed regions are marked by stars. We refrain from showing the best-fit points in each panel of Fig. 2, since the χ^2 is often relatively flat around the minimum (except for the combination of several data), and the best-fit point is not particularly informative. We give the best-fit coordinates only for the combination of all data.

In the first four panels of Fig. 2 (left to right, top to bottom) we display the parameter regions individually allowed by the four sub-GeV experiments, Fréjus, NUSEX, IMB, and Kamiokande. The Fréjus and NUSEX experiments are consistent with no oscillations, and thus strongly disfavor the situation of maximal mixing ($\psi \simeq \pi/4$), at least for not too small m^2 where they are not sensitive to oscillations. The IMB and Kamiokande experiments are instead compatible with large mixing in a wide range of m^2 ($m^2 \gtrsim 10^{-4} \text{ eV}^2$), although the best fit is not reached exactly for maximal mixing.

It should be noted that the sub-GeV experiments have still some sensitivity to values of m^2 as small as 10^{-4} eV^2 (see, e.g., [17,25,29]). For instance, the neutrino phase variation due to oscillations can be of $\mathcal{O}(1)$ for $E_\nu = 1 \text{ GeV}$, $m^2 = 10^{-4} \text{ eV}^2$, and a path length equal to the earth diameter. This fact, combined with our conservative error estimates, explains the extension of the IMB and Kamiokande allowed regions down to values as small as $m^2 \simeq 10^{-4} \text{ eV}^2$ in Fig. 2. Our Kamiokande allowed regions are larger than those derived by the Kamiokande collaboration analysis [4]. However, one has to consider that we use only the published experimental information, while the Kamiokande collaboration uses energy-angle lepton distributions that are not published, and also adopts a rather different approach in the statistical analysis of the data [4].

The 5th and 6th panels in Fig. 2 show the constraints from the multi-GeV Kamiokande data, taken both unbinned and binned respectively. The sensitivity to small m^2 is lower than in the sub-GeV cases, since the average neutrino energy is higher. In the binned case (full information from the angular distribution), m^2 is bounded from above at 90% C.L. In fact, the measured angular distribution is inconsistent with the flat oscillation probability corresponding to averaged fast oscillations ($m^2 \rightarrow \infty$) [4].

In the 7th and 8th panels of Fig. 2, we combine the sub-GeV and multi-GeV (unbinned and binned) Kamiokande data. In the 9th panel all sub-GeV data are combined together. Notice that maximal mixing ($\psi \simeq \pi/4$) is strongly disfavored for $m^2 \gtrsim 10^{-2} \text{ eV}^2$, due to the inclusion of the Fréjus and NUSEX data in the fit. In the 10th panel we combine the sub-GeV data with the multi-GeV unbinned data. The multi-GeV unbinned data disfavor the lowest values of m^2 that would be allowed by the sub-GeV data alone.

In the 11th panel we combine sub-GeV and binned multi-GeV data. Therefore, this panel contains the maximum information from the atmospheric neutrino experiments (8 sub-GeV + 10 multi-GeV observables). The best-fit is reached at $(m^2, \tan^2 \psi) \simeq (5 \times 10^{-3} \text{ eV}^2, 0.63)$ and at the symmetric point $(m^2, \tan^2 \psi) \simeq (5 \times 10^{-3} \text{ eV}^2, 1/0.63)$. The best-fit value of m^2 is somewhat lower than the popular value 10^{-2} eV^2 , since we include the Fréjus and NUSEX data. These data are compatible with $m^2 = 0$ (no oscillation) and thus tend to drag the m^2 -fit to lower values than those favored by IMB and Kamiokande alone. The value of the absolute χ^2 at the minimum is 19.7, which represents a good fit to the 18 atmospheric observables (with the freedom to vary only (m^2, ψ)). One should compare this value with the corresponding (worse) fit in the no-oscillation hypothesis, $\chi_{\text{no osc}}^2 = 44.6$.

The last panel in Fig. 2 shows the region allowed by the combination of all the established accelerator oscillation searches. The region allowed at 90% by all atmospheric neutrino data

is also allowed by present accelerator data (reactor data place no bounds in the $\nu_\mu \leftrightarrow \nu_e$ oscillation limit). The atmospheric bounds are in conflict with the accelerator bounds only at $\sim 99\%$ C.L. and high m^2 .

In Fig. 2, the magnitude of the theoretical neutrino flux error, σ_{flux} , has been taken equal to 30% (default value). This choice is not decisive in the fit, as shown in Fig. 3.

In Fig. 3 we compare two representative fits (all sub-GeV data, and all sub-GeV + multi-GeV data) using both $\sigma_{\text{flux}} = 30\%$ (solid contours) and $\sigma_{\text{flux}} = 15\%$ (dotted contours). The differences between the two cases are very small. In fact, since we include the proper correlations between the neutrino fluxes, the ν_e and ν_μ flux errors nearly “cancel” in the analysis, with a residual $\pm 5\%$ difference allowed in the relative ν_μ/ν_e flux normalization. Of course, a similar cancellation is reached by using the ratio $R_{\mu/e} = (\mu/e)_{\text{data}}/(\mu/e)_{\text{theory}}$, but with the serious disadvantage of obtaining a highly non-gaussian distribution for $R_{\mu/e}$ [10]. Previous analyses of the atmospheric neutrino anomaly that applied gaussian statistics to $R_{\mu/e}$, including our works [28] and [29], may thus have overestimated the statistical significance of the anomaly, and underestimated the mass-mixing regions allowed by the oscillation hypothesis.

In this work we have not analyzed the so-called upward-going muon data. These data are essentially consistent with no oscillations [31], although with large, non-cancelable flux errors—there are no “upward-going electrons” to be used for comparison. Thus we expect that, in a combined analysis: (1) the upward-going muon data should have a smaller statistical weight than the atmospheric data considered here, which should drive the fit; and (2) the inclusion of upward muon data should anyway disfavor a too strong suppression of the muon rates. This implies that the fit discussed in this section should be generally worsened for nearly maximal mixing ($\psi \sim \pi/4$). The three-flavor analysis of upward-going muon data is in progress and will be presented in a separate paper.

B. Pure $\nu_\mu \leftrightarrow \nu_e$ oscillations

We recall that, in our framework, the subcase of pure $\nu_\mu \leftrightarrow \nu_e$ oscillations is reached in the limit $\psi \rightarrow \pi/2$, which leaves (m^2, ϕ) as relevant variables.

This limit is more complicated than the $\nu_\mu \leftrightarrow \nu_\tau$ limit, since matter effects are not decoupled. It follows that the intervals $\phi \in [0, \pi/4]$ and $\phi \in [\pi/4, \pi/2]$ are not physically equivalent, and the scenarios (a) and (b) shown in Fig. 1 are also not equivalent. However, in the $\nu_\mu \leftrightarrow \nu_e$ oscillation case there is an interesting symmetry: the physics in (b) is equivalent to the physics in (a), provided that ϕ is replaced by its complementary angle ($\phi \rightarrow \frac{\pi}{2} - \phi$). This symmetry (discussed in Appendix C) allows us to consider only one scenario, (a) for definiteness.

In Fig. 4, we show the results of our $\nu_\mu \leftrightarrow \nu_e$ oscillation analysis in scenario (a). The corresponding results in scenario (b) are obtained by looking at the same figure in a mirror. Since the panels in Fig. 4 ($\nu_\mu \leftrightarrow \nu_e$ case) are analogous to the panels in Fig. 2 ($\nu_\mu \leftrightarrow \nu_\tau$ case) we just highlight the differences between the results in Figs. 4 and 2.

At large m^2 , the maximal mixing value $\phi \simeq \pi/4$ is in general disfavored, since “too many” ν_μ ’s oscillate into ν_e ’s, the muon (electron) rate become too suppressed (enhanced), and thus the flavor anomaly is overbalanced by the oscillations. In Fig. 2 this situation

was also disfavored, but not as strongly, since in the $\nu_\mu \leftrightarrow \nu_\tau$ case the electron rates are unaffected by oscillations.

At small m^2 , the contours are affected by the earth matter effects that are also responsible for the asymmetry with respect to the axis $\phi = \pi/4$. Notice that, in general, values of m^2 close to 10^{-4} eV² are more disfavored than in Fig. 2.

The combination of all data is shown in the 11th panel of Fig. 4 (all sub-GeV and multi-GeV binned). The allowed region should be compared with the constraints coming from accelerator and reactor searches. These constraints essentially exclude the upper part of the region preferred by atmospheric ν data, but are compatible with the (larger) lower part.

The best-fit for the combination of all data is obtained for $(m^2, \tan^2 \phi) = (6.6 \times 10^{-3} \text{ eV}^2, 0.36)$. For scenario (b), the best-fit would be obtained at the symmetric point $(m^2, \tan^2 \phi) = (6.6 \times 10^{-3} \text{ eV}^2, 1/0.36)$. The value of χ^2 at the minimum is $\chi_{\min}^2 = 15.6$, about 4 units lower than in the case of $\nu_\mu \leftrightarrow \nu_\tau$ oscillations ($\chi_{\min}^2 = 19.7$). Therefore $\nu_\mu \leftrightarrow \nu_e$ oscillations appear to be preferred to $\nu_\mu \leftrightarrow \nu_\tau$ oscillations in our global analysis.

The preference for the $\nu_\mu \leftrightarrow \nu_e$ case is essentially driven by the multi-GeV data. In Fig. 5, we show the measured and expected μ -like and e -like event rates in the five zenith-angle bins used by the Kamiokande collaboration for the multi-GeV data. The μ and e rates have been conventionally divided by their theoretical (central) value in absence of oscillations, μ_0 and e_0 (see also Ref. [10] where we introduced this graph). The ellipses represent 1σ contours ($\Delta\chi^2 = 1$).

The first of the horizontal panels in Fig. 5 refers to the no-oscillation case, which is clearly a bad fit to the data. The second panel refers to the best-fit to multi-GeV data with pure $\nu_\mu \leftrightarrow \nu_\tau$ oscillations. In this case, only the theoretical muon rates can vary, and the fit is not particularly good, although certainly better than in the no-oscillation case. The third panel refers to pure $\nu_\mu \leftrightarrow \nu_e$ oscillations. In this case, both μ and e rates vary with oscillations, and one can get higher theoretical electron rates that match better the experimental data (notice in particular the good fit in the first bin). The fourth panel refers to the general case of three-flavor oscillations, with (m^2, ψ, ϕ) unconstrained. The 3ν best-fit is only slightly better than in the $\nu_\mu \leftrightarrow \nu_e$ case. The differences between the overall fits in the third and fourth panels are only appreciable numerically and not by eye. In conclusion, $\nu_\mu \leftrightarrow \nu_e$ oscillations seem to provide a close-to-optimal fit to multi-GeV data.

In Fig. 6 we illustrate the importance of including the earth electron density in $\nu_\mu \leftrightarrow \nu_e$ oscillations. Figure 6 is analogous to Fig. 4 but *without* matter effects. The allowed regions in Fig. 6 and Fig. 4 differ considerably for low m^2 ; when matter effects are included (Fig. 4) the lowest values of m^2 do not provide a good fit [48]. The reason is that for not too small $\nu_\mu \leftrightarrow \nu_e$ mixing (i.e., for $\tan^2 \phi \sim 0.1\text{--}10$), the mixing angle in matter is rapidly suppressed for $m^2 \rightarrow 0$ [see Eq. (C4)], and so are the oscillations that should solve the flavor anomaly.

V. THREE-FLAVOR ANALYSIS IN THE $(m^2, \tan^2 \psi, \tan^2 \phi)$ PARAMETER SPACE

In this section we show the results of our analysis of atmospheric neutrino data within the three-flavor framework discussed in Sec. III. The free parameters of the fit are (m^2, ψ, ϕ) . The analysis includes all the sub-GeV data and the binned multi-GeV data. We represent

the results in the mixing-mixing plane $(\tan^2 \psi, \tan^2 \phi)$ at representative values of m^2 , in both scenarios (a) and (b) of Fig. 1.

A. Scenario (a)

In Fig. 7 we show the results of the fit to all the atmospheric data in scenario (a). The solid (dotted) lines represent sections, at given values of m^2 , of the three-dimensional $(m^2, \tan^2 \psi, \tan^2 \phi)$ manifold allowed by the fit at 90% C.L. (99% C.L.) for $N_{\text{DF}} = 3$ ($\Delta\chi^2 = 6.25$ and 11.34 respectively).

The representative values of m^2 range from 0.18 eV^2 down to $3.2 \times 10^{-4} \text{ eV}^2$. For $m^2 \gtrsim 10^{-2} \text{ eV}^2$ (first six panels), reactor and accelerator neutrino oscillation experiments also place bounds on the mixing angles. These bounds are discussed separately in Sec. V C.

We recall that in each panel of Fig. 7 the right-hand side corresponds (asymptotically) to the limit of pure $\nu_\mu \leftrightarrow \nu_e$ oscillations, and the lower side to pure $\nu_\mu \leftrightarrow \nu_\tau$ oscillations. The left-hand side, corresponding to pure $\nu_e \leftrightarrow \nu_\tau$ oscillations, never represents an acceptable fit to the data. The asymptotic regime is already reached at the ends of the $\tan^2 \psi$ and $\tan^2 \phi$ ranges adopted in Fig. 7.

The best three-flavor fit is reached at $(m^2, \tan^2 \psi, \tan^2 \phi) = (4.6 \times 10^{-3} \text{ eV}^2, 7.07, 0.28)$. The corresponding value of the χ^2 is $\chi^2_{\text{min}} = 14.8$, which represents a good fit to the 18 atmospheric observables, given the freedom of varying the three parameters (m^2, ψ, ϕ) .

At 90% C.L. there are both an upper and a lower bound on m^2 : $0.6 \times 10^{-3} \lesssim m^2 \lesssim 1.5 \times 10^{-1} \text{ eV}^2$. The upper bound, provided by the inclusion of multi-GeV data, however, disappears at $\sim 95\%$ C.L. (see below). The inclusion of laboratory oscillation data would make the upper bound tighter ($m^2 \lesssim 6 \times 10^{-2} \text{ eV}^2$ at 90% C.L., see Sec. V C).

For relatively large m^2 ($m^2 \gtrsim 2 \times 10^{-2} \text{ eV}^2$) the situations of maximal $\nu_\mu \leftrightarrow \nu_e$ mixing $[(\tan^2 \psi, \tan^2 \phi) = (\infty, 1)]$, of maximal $\nu_\mu \leftrightarrow \nu_\tau$ mixing $[(\tan^2 \psi, \tan^2 \phi) = (1, 0)]$, and of threefold maximal mixing $[(\tan^2 \psi, \tan^2 \phi) = (1, 1/2)]$, are not allowed. All these twofold and threefold maximal mixing situations are allowed, however, in the range $1.5 \times 10^{-3} \lesssim m^2 \lesssim 7 \times 10^{-3} \text{ eV}^2$ (at least). In this range, the vacuum oscillation probabilities for threefold maximal mixing [40,41] get significant corrections when matter effects are included (see Appendix C).

In many panels of Fig. 7, the allowed region interpolates smoothly between the two-flavor oscillation limits $\nu_\mu \leftrightarrow \nu_\tau$ and $\nu_\mu \leftrightarrow \nu_e$ [20–23,15]. However, for $m^2 \gtrsim 2 \times 10^{-2} \text{ eV}^2$, pure $\nu_\mu \leftrightarrow \nu_\tau$ oscillations are disfavored since the global fit improves towards the $\nu_\mu \leftrightarrow \nu_e$ oscillation limit.

The limits on m^2 for unconstrained ϕ and ψ are particularly interesting as guidelines for future long-baseline neutrino oscillation searches. In Fig. 8 we thus show the value of $\Delta\chi^2$ as a function of m^2 only (ψ and ϕ are projected away). The solid line refers to the default flux error ($\sigma_{\text{flux}} = 30\%$). The dashed line, which refers to $\sigma_{\text{flux}} = 20\%$, is not significantly different from the solid line.

From Fig. 8 one can trace the upper and lower bounds on m^2 placed by all the atmospheric neutrino data at any given C.L. However, for $m^2 \rightarrow \infty$ the $\Delta\chi^2$ tends to the asymptotic limit ~ 7 (not shown). It follows that, in the adopted three-flavor framework, atmospheric neutrinos place no upper bound on m^2 at 95% C.L. ($N_{\text{DF}} = 3$). Atmospheric neutrino

data would also not place any upper bound on m^2 if the zenith-angle dependence of the multi-GeV data were discarded, i.e. if *unbinned* multi-GeV data were used in the fit.

B. Scenario (b)

In Fig. 9 we show the results of the fit to all the atmospheric data in scenario (b) of Fig. 1. Figure 9 is analogous to Fig. 7, but all the calculations have been done with $-m^2$ instead of $+m^2$. The solid (dotted) lines represent sections, at given values of $-m^2$, of the three-dimensional $(m^2, \tan^2 \psi, \tan^2 \phi)$ manifold allowed by the data at 90% C.L. (99% C.L.) for $N_{\text{DF}} = 3$.

In scenario (b), the best-fit point is $(m^2, \tan^2 \psi, \tan^2 \phi) = (6.8 \times 10^{-3} \text{ eV}^2, 11.2, 2.82)$. The corresponding value of χ^2_{min} is 15.1, which is almost as good as in scenario (a).

As expected from symmetry arguments (see Appendix C), Fig. 9 and Fig. 7 coincide in the limit of pure $\nu_\mu \leftrightarrow \nu_\tau$ oscillations (lower side of each panel). In the limit of pure $\nu_\mu \leftrightarrow \nu_e$ oscillations (right side of each panel) these figures coincide⁵ modulo the replacement $\phi \rightarrow \frac{\pi}{2} - \phi$. In the intermediate, genuine three-flavor mixing cases, the bounds shown in Figs. 9 and 7 are slightly different at any m^2 .

The differences between the three-flavor fits in Figs. 7 and 9 are not unexpected, since they correspond to two physically different scenarios. Unfortunately, the differences are quite small, implying that the available information on atmospheric neutrinos is not sufficiently accurate to discriminate the two cases (a) and (b). A significant discrimination would have important implications. For instance a hypothetical, pronounced preference of atmospheric data for scenario (a) would support the theoretical prejudice that the spectrum of neutrino masses is similar to the spectrum of charged fermions (two light states and a third, much heavier state). It will be interesting to see if the atmospheric neutrino data that are being collected with high statistics by the running SuperKamiokande experiment will show a preference for one of the two scenarios (if they confirm the flavor anomaly). We recall that this information cannot be provided either by accelerator,⁶ reactor, or solar neutrino oscillation searches, i.e., these experiments *a priori* do not distinguish the scenarios (a) and (b) at zeroth order in $\delta m^2/m^2$.

Finally, we complete our survey of the fit in scenario (b) by showing in Fig. 10 the dependence of $\Delta\chi^2$ on $-m^2$. Fig. 10 is the analogous to Fig. 8 in scenario (b).

⁵ The coincidence of the C.L. contours in these two-flavor limits is not perfectly realized because the best-fit point and the value of the χ^2 at the minimum are not exactly equal (and are not expected to be equal) in scenarios (a) and (b).

⁶ However, futuristic accelerator oscillation searches with extremely long baselines (greater than 10^3 km) could in principle probe the difference between scenarios (a) and (b) through earth matter effects.

C. Comparison with other oscillation searches

The three-flavor bounds shown in Figs. 7 and 9 and discussed in Sections V A and V B were obtained by fitting only the atmospheric neutrino data. In this section, we show their interplay with the independent constraints obtained by accelerator and reactor neutrino oscillation searches [15] and by solar neutrino experiments [16].

The analyses [15] and [16] were performed under the same assumption on the neutrino spectrum shown in Fig. 1, namely that the two independent neutrino mass squared differences, $\delta m^2 = |m_2^2 - m_1^2|$ and $m^2 = |m_3^2 - m_2^2|$, are largely separated: $\delta m^2 \ll m^2$. Accelerator and reactor neutrinos were assumed to probe, as the atmospheric neutrinos, the dominant square mass difference m^2 , as the slow oscillations driven by δm^2 were effectively frozen. Conversely, solar neutrinos were assumed to probe the subdominant square mass difference δm^2 , as the fast oscillations driven by m^2 were effectively averaged out. The parameter spaces probed by terrestrial (accelerator, reactor, and atmospheric) neutrinos and by solar neutrinos have been discussed thoroughly in [15] and [16].

In Fig. 11, we show the bounds coming from the established accelerator and reactor oscillation searches [15] (the recent data from the Liquid Scintillator Neutrino Detector (LSND) experiment [49] are not included). These negative searches exclude horizontal bands in the $(\tan^2 \psi, \tan^2 \phi)$ plane for $m^2 \gtrsim 10^{-2} \text{ eV}^2$ (90% C.L. limits are shown). Superposed are the 90% C.L. regions from the atmospheric neutrino analysis (only in scenario (a) for definiteness). The $\nu_\mu \leftrightarrow \nu_e$ oscillation limit (right side of the panels) is generally disfavored in the range probed by laboratory oscillation experiments, mainly because it is not consistent with the unsuccessful ν_e disappearance searches at reactors. For $m^2 \gtrsim 6 \times 10^{-2} \text{ eV}^2$ the atmospheric data are not compatible with existing laboratory limits at any ψ or ϕ . For $m^2 \lesssim 10^{-2} \text{ eV}^2$, however, there are no laboratory constraints on neutrino mixing, and the fits to atmospheric data (six lowest panels of Figs. 7 and 9) are unaffected.

In conclusion, the limits placed by the combination of accelerator, reactor, and atmospheric neutrino data on m^2 in our three-flavor framework are $6 \times 10^{-4} \text{ eV}^2 \lesssim m^2 \lesssim 6 \times 10^{-2} \text{ eV}^2$ (90% C.L., $N_{\text{DF}} = 3$). Future long-baseline experiments will be able to explore a large fraction of this m^2 range.

Concerning solar neutrinos, we have emphasized in [16] that they probe the same mixing angle ϕ probed by terrestrial (atmospheric, accelerator and reactor) neutrino experiments. If one accepts the explanation of solar neutrino deficit provided by matter-enhanced oscillations, then the data constrain ϕ in the range $\tan^2 \phi \lesssim 1.4$ at 90% C.L. ($N_{\text{DF}} = 3$), with a preference for the value $\tan^2 \phi = 0$ [16]. These bounds coming from solar ν data exclude significant parts of the large- ϕ regions allowed by atmospheric neutrino data in Figs. 4, 7, 9, and 11. This should be taken into account when building models of neutrino masses and mixings which try to accommodate both the solar neutrino deficit and the atmospheric neutrino anomaly.

In our framework, once δm^2 is fixed by solar neutrinos, it is not possible to explain both the atmospheric neutrino anomaly and the recent LSND evidence [49] for oscillations with the remaining mass parameter m^2 . We have shown previously that atmospheric neutrino data alone place an upper limit to m^2 of about $1.5 \times 10^{-1} \text{ eV}^2$, which is strengthened to $m^2 \lesssim 6 \times 10^{-2} \text{ eV}^2$ when accelerator and reactor data are included. The range $m^2 \lesssim 6 \times 10^{-2} \text{ eV}^2$ is too low for significant neutrino oscillation effects at LSND. It follows that, in our

framework, one can either fit the atmospheric neutrino anomaly or the LSND event excess, but not both. We intend to examine the second option (fit to LSND data) in a separate publication; some interesting results were already obtained with older LSND data in [15] (see there Figs. 11 and 12 and the related discussion). However, it should be noted that the atmospheric data fit at large m^2 is essentially driven by the angular distribution of multi-GeV events observed in Kamiokande. If this information were discarded, i.e., if one used only unbinned multi-GeV data, then atmospheric neutrino data alone would not place an upper bound on m^2 , and one could find [50] a very small region of the parameter space which is marginally allowed by both LSND and sub-GeV atmospheric data, as well by present accelerator and reactor constraints. This solution is admittedly fragile [50].

A final remark is in order. The basic assumption underlying this work and Refs. [15,16] is that $\delta m^2 \ll m^2$ (Fig. 1). Then all the calculations are done at zeroth order in $\delta m^2/m^2$, i.e., one takes $\delta m^2 = 0$ and m^2 finite for terrestrial neutrino oscillations, and δm^2 finite and $m^2 = \infty$ for solar neutrino oscillations. If δm^2 is close to the best-fit to solar neutrino data ($\delta m^2 \sim 5 \times 10^{-6} \text{ eV}^2$) and if m^2 is close to the best-fit to atmospheric neutrino data ($m^2 \sim 0.6 \times 10^{-2} \text{ eV}^2$) then $\delta m^2/m^2 \sim 10^{-3}$ and the zeroth order approximation is certainly adequate. In Ref. [29] we have numerically shown that for $\delta m^2/m^2$ as high as 1/10 the leading first-order corrections to the zeroth approximation do not alter substantially the results of both the solar and the atmospheric neutrino data fit. However, if one takes the *highest* values of δm^2 allowed by solar neutrinos ($\delta m^2 \sim 1.5 \times 10^{-4} \text{ eV}^2$) [16] and the *lowest* values of m^2 allowed by atmospheric neutrinos ($m^2 \sim 6 \times 10^{-4} \text{ eV}^2$) at 90% C.L., then the ratio $\delta m^2/m^2$ is about 1/4, so that the two squared mass differences are not well-separated, and our approximations become very rough. Such a contrived situation seems improbable, but if it were realized in nature, then one should necessarily resort to the most general three-flavor formalism to analyze it.

VI. SUMMARY AND CONCLUSIONS

In this work we have analyzed the available experimental data on the anomalous flavor composition of the atmospheric neutrino flux with three-flavor neutrino oscillations. Data on upward-going muons are not included and will be examined in a separate work.

The adopted theoretical framework is characterized by one dominant neutrino square mass difference, m^2 . The neutrino mass spectrum can assume either form (a) or (b) of Fig. 1. Scenarios (a) and (b) are physically different when neutrino oscillations in the earth matter background are considered. In both cases the variables relevant to atmospheric neutrino oscillations are m^2 and two mixing angles, ψ and ϕ .

We have performed a global analysis of all data, and found the regions of the (m^2, ψ, ϕ) parameter space in which three-flavor neutrino oscillations are consistent with the available data. In particular, we have included in the analysis the neutrino-induced e -like and μ -like event rates measured in four sub-GeV experiments, Fréjus, NUSEX, Kamiokande, and IMB, as well as the lepton rates measured in the five zenith-angle sectors of the multi-GeV Kamiokande experiment, for a total of 18 observables in the fit. We have made accurate calculations of the expected muon and electron rates in the various detectors, taking into account the differential energy-angle distribution of the (anti)neutrino fluxes, the differential

(anti)neutrino interaction cross-sections, and the detector efficiencies. We have paid particular attention to the statistical analysis, which includes the proper correlations among the experimental and theoretical errors. The oscillation probabilities have been calculated in the three-flavor framework defined by Fig. 1, including the earth matter effect in the evolution of the neutrino flavor states. The main results of our analysis are shown in Fig. 7 for scenario (a) and in Fig. 9 for scenario (b). Three-flavor neutrino oscillations provide a good fit to the 18 data (with three free parameter), as the minimum χ^2 is ~ 15 in both cases.

We have also analyzed in detail the subcases of two-flavor $\nu_\mu \leftrightarrow \nu_\tau$ oscillations (Fig. 2) and $\nu_\mu \leftrightarrow \nu_e$ oscillations (Fig. 4). The analysis of these subcases provided us with valuable information on the relative weight and influence of the different pieces of data in the global fit, as well as on the importance of the earth matter effect (as derived by comparing Fig. 4 and Fig. 6). The Kamiokande multi-GeV data are fitted better in the $\nu_\mu \leftrightarrow \nu_e$ case than in the $\nu_\mu \leftrightarrow \nu_\tau$ case, as shown in Fig. 5, although more data are needed to confirm this indication. In particular, the upcoming data from the running SuperKamiokande experiment [13] will certainly help in clarifying the atmospheric neutrino anomaly and its implications in terms of neutrino properties.

We have compared the region preferred by atmospheric neutrino data with the bounds coming from negative oscillation searches at accelerator and reactors [15] in Fig. 11. These bounds exclude a large part of the region allowed by atmospheric data (especially in the limit of pure $\nu_\mu \leftrightarrow \nu_e$ oscillations) for $m^2 \gtrsim 10^{-2}$ eV². For $m^2 \lesssim 10^{-2}$ eV² there are no significant bounds from reactor data and the atmospheric data fit is unaffected. In particular, for $m^2 \lesssim 10^{-2}$ eV² the threefold maximal mixing scenario [40,41] is allowed by the data. It must be added, however, that threefold maximal mixing is not supported by the independent analysis of all solar neutrino data [16].

In Sec. V C we have also discussed the interplay between atmospheric and solar neutrino results. Solar neutrino data place an upper bound on ϕ [16] that further constrains the atmospheric results at any m^2 . The value of m^2 needed to fit atmospheric neutrino data is not compatible, within this framework, with the possible recent indication for neutrino oscillations coming from the LSND experiment [49]. A marginal compatibility between the LSND data and the atmospheric anomaly might be reached [50] if the information coming from the zenith-angle distribution of multi-GeV event is discarded.

This work is part of a wider research programme in which we intend to analyze, in the same three-flavor framework, the world data related to neutrino oscillations. We have analyzed so far the results coming from 14 experiments: 3 accelerator experiments (CERN CDHSW, Fermilab E531, and BNL E776) [15], 3 reactor experiments (Bugey, Gösgen, and Krasnoyarsk reactors) [15], 4 solar neutrino experiments (Homestake, GALLEX, SAGE, and Kamiokande) [16], and 4 atmospheric neutrino experiments (Fréjus, NUSEX, IMB, and Kamiokande, this work). (See also [28,29].) We have discussed in [15] some implications of older LSND results [51], and in [14] the tests of three-flavor mixing in future long-baseline neutrino oscillation experiments. We hope that the three-flavor framework adopted in these works can become a popular way of analyzing or even presenting the experimental results or expectations, instead of the usual two-generation approach which is unable to accommodate more than one oscillation channel at a time.

ACKNOWLEDGMENTS

We thank C. Giunti and P. I. Krastev for useful discussions. We are grateful to J. Pantaleone for reading the manuscript and for very helpful comments. G.L.F. would like to thank Prof. Milla Baldo Ceolin and the organizers of the VII Workshop *Neutrino Telescopes '96* (Venice, Italy, feb. 1996), where preliminary results of this work were presented. The work of E.L. was supported in part by INFN and in part by a Hansmann membership at the Institute for Advanced Study. This work was performed under the auspices of the European Theoretical Astroparticle Network (TAN).

APPENDIX A: TREATMENT OF KAMIOKANDE MULTI-GeV DATA

In this appendix we describe in detail our treatment of the Kamiokande multi-GeV data.

The analysis of the Kamiokande multi-GeV data [4] depends crucially upon the distribution of lepton events (N_β) of given flavor β as a function of the zenith angle θ . In the presence of neutrino oscillations, β -flavor lepton events may be initiated by neutrinos of original flavor α , and the angular distribution can be expressed as:

$$\frac{dN_\beta}{d\theta} = \sum_\alpha \int_{E_\nu^{\min}}^\infty dE_\nu \frac{d^2\Phi_\alpha}{dE_\nu d\theta} P_{\alpha\beta} \int_{E_\ell^{\min}}^{E_\nu} dE_\ell \frac{d\sigma_\beta}{dE_\ell} \varepsilon_\beta , \quad (\text{A1})$$

where:

$$\begin{aligned} \frac{dN_\beta(\theta)}{d\theta} &= \text{lepton angular distribution} , \\ E_\nu &= \text{neutrino energy} , \\ E_\ell &= \text{lepton energy} , \\ \frac{d^2\Phi_\alpha(E_\nu, \theta)}{dE_\nu d\theta} &= \text{distribution of unoscillated } \nu_\alpha , \\ P_{\alpha\beta}(E_\nu, \theta) &= \text{flavor oscillation probability} , \\ \frac{d\sigma_\beta(E_\ell)}{dE_\ell} &= \text{differential } \nu_\beta \text{ cross section} , \\ \varepsilon_\beta(E_\ell) &= \text{lepton detection efficiency} . \end{aligned} \quad (\text{A2})$$

For the sake of simplicity (and of computing time) in Eq. (A1) we have assumed that the lepton direction θ is the same as the incident neutrino direction θ_ν , $\theta \simeq \theta_\nu$. Actually, in the Kamiokande multi-GeV data sample, the typical difference is $\sqrt{\langle(\theta - \theta_\nu)^2\rangle} \simeq 15^\circ\text{--}20^\circ$ [4]. We simulate the effect of the $\theta\text{--}\theta_\nu$ difference by smearing the distribution $dN_\beta/d\theta$ in Eq. (A1) with a Gaussian distribution having a one-sigma width of $\sim 17^\circ$.

The evaluation of the inner integral in Eq. (A1) requires detailed experimental information that is not available. In particular, the lepton detection efficiency function $\varepsilon_\beta(E_\ell)$, which includes the intrinsic detector acceptance and the analysis cuts, is not published for multi-GeV data [4]. A worse problem is due to the impossibility of defining, event by event, the lepton energy E_ℓ for tracks that are not fully contained. For these (partially contained)

higher-energy events, the intrinsic “total” energy can be associated with the released “visible” lepton energy on a statistical basis only, by means of a detailed simulation of the Kamiokande detector (which is beyond our possibilities and interests). However, the ignorance of such experimental ingredients can be overcome by re-writing Eq. (A1) in terms of the simulated energy spectrum of the parent neutrinos (which embeds all these effects) as published in [4].

The method is the following. The (E_ν, θ) -distribution of unoscillated neutrinos can be factorized as:

$$\frac{d^2\Phi_\alpha(E_\nu, \theta)}{dE_\nu d\theta} = \frac{d\Phi'_\alpha(E_\nu)}{dE_\nu} \cdot \frac{d\Phi''_\alpha(E_\nu, \theta)}{d\theta}, \quad (\text{A3})$$

with the normalization

$$\int d\theta \frac{d\Phi''_\alpha(E_\nu, \theta)}{d\theta} = 1 \quad (\text{at any } E_\nu). \quad (\text{A4})$$

Applying the factorization of Eq. (A3) in Eq. (A1) one has that:

$$\begin{aligned} \frac{dN_\beta}{d\theta} &= \int dE_\nu \frac{d\Phi''_\alpha}{d\theta} P_{\alpha\beta} \frac{d\Phi'_\alpha}{dE_\nu} \int dE_\ell \frac{d\sigma_\beta}{dE_\ell} \varepsilon_\beta \\ &= \int dE_\nu \frac{d\Phi''_\alpha}{d\theta} P_{\alpha\beta} Q_{\alpha\beta} \frac{dn_\beta}{dE_\nu}, \end{aligned} \quad (\text{A5})$$

where

$$Q_{\alpha\beta}(E_\nu) = \frac{d\Phi'_\alpha}{dE_\nu} \left(\frac{d\Phi'_\beta}{dE_\nu} \right)^{-1} \quad (\text{A6})$$

is known from atmospheric flux calculations, and

$$\frac{dn_\beta(E_\nu)}{dE_\nu} = \frac{d\Phi'_\beta}{dE_\nu} \int dE_\ell \frac{d\sigma_\beta}{dE_\ell} \varepsilon_\beta \quad (\text{A7})$$

represents the energy distribution of the parent neutrinos that induce β -lepton events in the Kamiokande detector, integrated over the lepton spectrum.

As reference energy-angle neutrino flux distributions, we use the calculations of the Bartol group [34] smoothly connected to the Volkova calculations [52] at higher energies. This reference choice corresponds to the option “Flux B” in [4].

The function $dn_\beta(E_\nu)/dE_\nu$, that embeds all those experimental aspects of the lepton detection efficiency and energy reconstruction that we ignore, is published in Fig. 2(b) of Ref. [4]. Since both $d\Phi''_\alpha/d\theta$ and $Q_{\alpha\beta}$ are known, and $P_{\alpha\beta}$ is calculable in a given oscillation scenario, one finally has all the ingredients to calculate the angular distribution of lepton events from Eq. (A5).⁷

⁷ It should be added, however, that in this way our analysis of the multi-GeV data depends implicitly upon the neutrino cross sections as implemented in the Kamiokande Monte Carlo simulation.

In particular, we have computed the angular distribution of e -like and μ -like multi-GeV events in absence of oscillations ($P_{\alpha\beta} = \delta_{\alpha\beta}$). The results are shown in Fig. 12 as dashed lines. The solid lines represent the published Kamiokande simulation [4]. The agreement is very good, as the differences are smaller than the statistical uncertainties.

The author of Ref. [27] used independently a somewhat similar approach to the analysis of multi-GeV data but did not obtain, however, a good agreement with the published Kamiokande simulation of e -like events.

A final remark is in order. The functions $dn_\beta(E_\nu)/dE_\nu$ ($\beta = e, \mu$) reported in [4] include the contributions of both neutrinos and antineutrinos. However, it is important to separate the ν and $\bar{\nu}$ contributions, since $P(\nu_\alpha \rightarrow \nu_\beta) \neq P(\bar{\nu}_\alpha \rightarrow \bar{\nu}_\beta)$ when matter oscillations are considered. We make the reasonable assumption that $\varepsilon_\beta \simeq \varepsilon_{\bar{\beta}}$. Then, since the ratios of ν and $\bar{\nu}$ fluxes and cross sections are known at any energy, one can separate the distribution dn_β/dE_ν of parent *neutrinos* from the distribution $dn_{\bar{\beta}}/dE_\nu$ of parent *antineutrinos*.

APPENDIX B: CORRELATION OF ERRORS

In [10] we examined the various sources of uncertainties affecting the measured and expected e -like and μ -like event rates R_e and R_μ in the atmospheric neutrino experiments, together with their correlations. We were thus able, for any single experiment, to construct the covariance matrix of the residuals ($R_\alpha^{\text{theor}} - R_\alpha^{\text{expt}}$) and to perform a correct (Gaussian) statistical analysis of the atmospheric ν anomaly. As far as a single experiment is concerned, here we use the same approach.

However, when the information of two or more experiments is combined—as in the present work—one has also to take into account that the theoretical errors of the neutrino fluxes are highly correlated from experiment to experiment. For instance, a hypothetical systematic shift of +20% in the calculated (unoscillated) flux of sub-GeV ν_e 's propagates coherently to the expected rates of e -like events in *all* the sub-GeV experiments at the same time. Moreover, one also expects the μ -like event rates to increase by $\sim 20\%$ because of the tight correlation of calculated ν_e and ν_μ fluxes, with an allowance for a residual uncertainty (of about 5%) in the μ/e ratio.

Therefore, in constructing the covariance matrix for the observables analyzed in this work, we include the additional off-diagonal elements corresponding to the correlations of the neutrino flux uncertainties between any two experiments, and between any two bins of the Kamiokande multi-GeV data sample.⁸

More precisely, let us call (A, B) a generic couple of experiments (or couple of multi-GeV data bins). Then the correlations between the ν_e and ν_μ theoretical flux errors in A and B are given by:

$$\rho_{ee}(A, B) = 1 ,$$

⁸ In principle there could also be correlations among the *experimental* systematic uncertainties affecting any two bins of the Kamiokande multi-GeV data. However, for lack of published information [4] we ignore such additional correlations.

$$\begin{aligned}\rho_{\mu\mu}(A, B) &= 1, \\ \rho_{\mu e}(A, B) &= 1 - \frac{1}{2} \frac{\sigma_{\text{flux}}^2}{\sigma_{\text{ratio}}^2},\end{aligned}\tag{B1}$$

where σ_{flux} is the assumed fractional uncertainty in the overall flux normalization (e.g., $\pm 30\%$), and σ_{ratio} is the assumed residual uncertainty in the μ/e ratio (typically $\pm 5\%$, which we choose as default value). For instance, for $(\sigma_{\text{flux}}, \sigma_{\text{ratio}}) = (30\%, 5\%)$ the μ - e flux error correlation is $\rho_{\mu e} = 0.986$ [10].

We have decided, however, to ignore the correlations when A labels a sub-GeV observable *and* B labels a multi-GeV observable (or vice versa). In fact, the flux of low-energy and high-energy neutrinos are not necessarily correlated. A systematic shift of, e.g., $+20\%$ in the low-energy neutrino flux normalization does not necessarily imply the same shift at higher energy. This would happen, for instance, if the *slope* of the theoretical neutrino energy distribution were systematically biased. At present, we do not know how to relate the uncertainties affecting the low-energy and the high-energy fluxes of atmospheric neutrinos, and thus ignore their possible correlations in the χ^2 statistics.

The inclusion of the (known) correlation effects in any single experiment, as well as in the combination of all the experimental data, is a distinguishing feature of our analysis.

APPENDIX C: SYMMETRIES OF THE OSCILLATION PROBABILITY

In this appendix we discuss several symmetry properties of the neutrino and antineutrino oscillation probabilities under given transformations of the neutrino masses and mixing, in the two scenarios (a) and (b) of Fig. 1. These properties are useful to understand the results of the analysis of the atmospheric neutrino data. In particular, we show that the scenarios (a) and (b) are not equivalent when the earth matter effects are included in the (anti)neutrino propagation.

We recall that we always assume m^2 positive ($m^2 = |m^2|$), and that the two scenarios (a) and (b) are distinguished by the overall sign of m^2 : (a) \rightarrow (b) $\iff +m^2 \rightarrow -m^2$. It is useful to set conventionally the zero of the neutrino squared mass scale halfway between the doublet (ν_1, ν_2) and the “lone” state ν_3 shown in Fig. 1. With this position, the neutrino squared mass spectrum takes the form:

$$(m_1^2, m_2^2, m_3^2) = \begin{cases} (-\frac{m^2}{2}, -\frac{m^2}{2}, +\frac{m^2}{2}) & \text{scenario (a)} \\ (+\frac{m^2}{2}, +\frac{m^2}{2}, -\frac{m^2}{2}) & \text{scenario (b)} \end{cases}.\tag{C1}$$

Let us consider the following 8 transformations T_i :

$$\begin{aligned}T_1 : & \quad m^2 \rightarrow -m^2 & \text{at any } \psi, \phi ; \\ T_2 : & \quad (m^2, \phi) \rightarrow (m^2, \pi/2 - \phi) & \text{at } \psi = 0 ; \\ T_3 : & \quad (m^2, \phi) \rightarrow (m^2, \pi/2 - \phi) & \text{at } \psi = \pi/2 ; \\ T_4 : & \quad (m^2, \psi) \rightarrow (m^2, \pi/2 - \psi) & \text{at } \phi = 0 ; \\ T_5 : & \quad (m^2, \phi) \rightarrow (-m^2, \pi/2 - \phi) & \text{at } \psi = 0 ; \\ T_6 : & \quad (m^2, \phi) \rightarrow (-m^2, \pi/2 - \phi) & \text{at } \psi = \pi/2 ; \\ T_7 : & \quad (m^2, \psi) \rightarrow (-m^2, \pi/2 - \psi) & \text{at } \phi = 0 ; \\ T_8 : & \quad (\nu, m^2) \rightarrow (\bar{\nu}, -m^2) & \text{at any } \psi, \phi .\end{aligned}\tag{C2}$$

The transformation T_1 changes the overall sign of m^2 and thus maps scenario (a) into (b) or vice versa. The transformations $T_{2,5}$, $T_{3,6}$, and $T_{4,7}$ are relevant respectively for the subcases of pure two-flavor $\nu_e \leftrightarrow \nu_\tau$ oscillations ($\psi = 0$), $\nu_e \leftrightarrow \nu_\mu$ oscillations ($\psi = \pi/2$), and $\nu_\mu \leftrightarrow \nu_\tau$ oscillations ($\phi = 0$). The transformation T_8 interchanges neutrinos with antineutrinos and, at the same time, changes the sign of m^2 . Notice that the T_i 's in Eq. (C2) are not all independent: $T_5 = T_1 \cdot T_2$, $T_6 = T_1 \cdot T_3$, and $T_7 = T_1 \cdot T_4$.

We prove the following statements: (1) in vacuum, the oscillation probabilities are invariant under T_1 , T_2 , T_3 , T_4 , T_5 , T_6 , T_7 , and T_8 ; (2) in matter, the oscillation probabilities are invariant only under T_4 , T_5 , T_6 , T_7 , and T_8 ; (3) in matter, the additional symmetries T_1 , T_2 , and T_3 are restored in the limit $m^2 \rightarrow \infty$.

The statement (1) is evident from inspection of the vacuum oscillation probabilities (equal for neutrinos and antineutrinos):

$$\begin{aligned}
P_{ee}^{\text{vac}} &= 1 - 4s_\phi^2 c_\phi^2 S, \\
P_{\mu\mu}^{\text{vac}} &= 1 - 4c_\phi^2 s_\psi^2 (1 - c_\phi^2 s_\psi^2) S, \\
P_{\tau\tau}^{\text{vac}} &= 1 - 4c_\phi^2 c_\psi^2 (1 - c_\phi^2 c_\psi^2) S, \\
P_{e\mu}^{\text{vac}} &= 4s_\phi^2 c_\phi^2 s_\psi^2 S, \\
P_{e\tau}^{\text{vac}} &= 4s_\phi^2 c_\phi^2 c_\psi^2 S, \\
P_{\mu\tau}^{\text{vac}} &= 4c_\phi^4 s_\psi^2 c_\psi^2 S,
\end{aligned} \tag{C3}$$

where $S = \sin^2(m^2 x / 4E_\nu)$. Note that the angles ω and δ never appear in Eq. (C3). Of course, $P_{\alpha\beta} = P_{\beta\alpha}$.

The probabilities in Eq. (C3) are invariant under T_1 , implying that the cases (a) and (b) are indistinguishable in vacuum. The symmetries T_2 and T_5 imply that the parameters of pure $\nu_e \leftrightarrow \nu_\tau$ oscillations in vacuum can be restricted to the case $+m^2$ and $\phi \in [0, \pi/4]$, as the cases $-m^2$ $\phi \in [\pi/4, \pi/2]$ become equivalent. Analogously, this is true for pure $\nu_e \leftrightarrow \nu_\mu$ or $\nu_\mu \leftrightarrow \nu_\tau$ oscillations in vacuum.

When matter effects are included, the situation becomes more complicated [23] and several symmetries are broken. For the sake of simplicity, we discuss the symmetry properties of the oscillation probabilities in the case of constant electron density, $N_e = \text{const}$. Our conclusions are also valid for a generic $N_e = N_e(x)$, but the proof is considerably more involved and less transparent, since the neutrino propagation equations are not analytically integrable for a generic density. Instead, for constant N_e the oscillation probabilities can be expressed in compact form. For *neutrinos* they are given by (we omit the derivation):

$$\begin{aligned}
P_{ee} &= 1 - 4s_\Phi^2 c_\Phi^2 S_{31}, \\
P_{\mu\mu} &= 1 - 4s_\Phi^2 c_\Phi^2 s_\psi^4 S_{31} - 4s_\Phi^2 s_\psi^2 c_\psi^2 S_{21} - 4c_\Phi^2 s_\psi^2 c_\psi^2 S_{32}, \\
P_{\tau\tau} &= 1 - 4s_\Phi^2 c_\Phi^2 c_\psi^4 S_{31} - 4s_\Phi^2 s_\psi^2 c_\psi^2 S_{21} - 4c_\Phi^2 s_\psi^2 c_\psi^2 S_{32}, \\
P_{e\mu} &= 4s_\Phi^2 c_\Phi^2 s_\psi^2 S_{31}, \\
P_{e\tau} &= 4s_\Phi^2 c_\Phi^2 c_\psi^2 S_{31}, \\
P_{\mu\tau} &= -4s_\Phi^2 c_\Phi^2 s_\psi^2 c_\psi^2 S_{31} + 4s_\Phi^2 s_\psi^2 c_\psi^2 S_{21} + 4c_\Phi^2 s_\psi^2 c_\psi^2 S_{32},
\end{aligned} \tag{C4}$$

where Φ is the effective mixing angle ϕ in matter (ψ remains unchanged):

$$\sin 2\Phi = \frac{\sin 2\phi}{\sqrt{(\cos 2\phi \mp A/m^2)^2 + (\sin 2\phi)^2}}. \quad (\text{C5})$$

In Eq. (C4) the oscillating factors S_{ij} are defined as

$$S_{ij} = \sin^2 \left(\frac{M_i^2 - M_j^2}{4E_\nu} x \right), \quad (\text{C6})$$

where M_i^2 are the neutrino square mass eigenvalues in matter,

$$\begin{aligned} M_1^2 &= \mp \frac{m^2}{2} \frac{s_{2\phi}}{s_{2\Phi}} + \frac{A}{2}, \\ M_2^2 &= \mp \frac{m^2}{2}, \\ M_3^2 &= \pm \frac{m^2}{2} \frac{s_{2\phi}}{s_{2\Phi}} + \frac{A}{2}, \end{aligned} \quad (\text{C7})$$

and $A = 2\sqrt{2}G_F N_e E_\nu$ is the matter-induced square mass term. We recall that the neutrino square mass eigenvalues in vacuum are given in Eq. (C1).

In Eqs. (C5)–(C7) the upper sign refer to scenario (a) and the lower sign to scenario (b). Notice that, as in the vacuum case, the angles ω and δ never appear in the oscillation probabilities in Eq. (C4).

From Eqs. (C4)–(C7) it follows that the earth matter effects do not vanish for threefold maximal mixing, corresponding to $(\tan^2 \psi, \tan^2 \phi) = (1, 1/2)$. In the interesting range $10^{-3} \text{ eV}^2 \lesssim m^2 \lesssim 10^{-2} \text{ eV}^2$, the matter corrections to the “vacuum” lepton rates can be as large as 10% in the sub-GeV case and as large as 30% in the multi-GeV case. The fits to the threefold maximal mixing scenario in [40,41] were performed neglecting matter effects.

The oscillation probabilities in Eq. (C4) are not invariant under the transformation T_1 . Therefore, the scenarios (a) and (b) are in general physically different for atmospheric neutrinos traversing the earth matter. The difference can be traced to the matter-induced neutrino mass term A [Eq. (C7)], which is positive both in (a) and (b), while the overall sign of the vacuum mass m^2 changes in the two scenarios.

However, the probabilities in Eq. (C4) are invariant under the transformations T_4 , T_5 , T_6 , and T_7 . Notice in particular that:

$$\begin{aligned} \psi = 0 \quad (\nu_e \leftrightarrow \nu_\tau) &\rightarrow P_{e\tau} = 4s_\Phi^2 c_\Phi^2 S', \\ \psi = \pi/2 \quad (\nu_e \leftrightarrow \nu_\mu) &\rightarrow P_{e\mu} = 4s_\Phi^2 c_\Phi^2 S', \\ \phi = 0 \quad (\nu_\mu \leftrightarrow \nu_\tau) &\rightarrow P_{\mu\tau} = 4s_\psi^2 c_\psi^2 S = P_{\mu\tau}^{\text{vac}}, \end{aligned} \quad (\text{C8})$$

where

$$S' = \sin^2 \left(\frac{m^2}{4E_\nu} \frac{s_{2\phi}}{s_{2\Phi}} x \right). \quad (\text{C9})$$

The symmetry T_3 does not apply to the probabilities in Eq. (C4). Therefore, the description of pure two-flavor oscillation $\nu_e \leftrightarrow \nu_\mu$ in matter cannot be exhausted by taking

$+m^2$ and $\phi \in [0, \pi/4]$. Either one takes $+m^2$ and extends the range of ϕ to $[0, \pi/2]$ (as in this work), or one keeps $\phi \in [0, \pi/4]$, but considers both $+m^2$ and $-m^2$ (as in [48]). Analogously, this is true for $\nu_e \leftrightarrow \nu_\tau$ oscillations in matter, which are not invariant under T_2 .

Notice that the symmetry T_4 , corresponding to $\psi \rightarrow \frac{\pi}{2} - \psi$ at given m^2 for pure $\nu_\mu \leftrightarrow \nu_\tau$ oscillations ($\phi = 0$), holds both in vacuum and in matter. In fact, matter effects are irrelevant for pure $\nu_\mu \leftrightarrow \nu_\tau$ oscillations.

Let us now consider the *antineutrino* oscillation probabilities. Equation (C3) holds both for neutrinos and antineutrino oscillations (in vacuum). Equation (C4) refers only to neutrinos. For antineutrinos, the matter-induced term A changes sign. However, if one also changes the sign of m^2 , the antineutrino propagation becomes equivalent to neutrino propagation. In other words, the oscillation probabilities of *neutrinos* in scenario (a) are equal to the oscillation probabilities of *antineutrinos* in scenario (b), and vice versa, as expressed by the symmetry T_8 . Notice that the higher symmetry $T_1 \cdot T_8$, which corresponds to $\nu \rightarrow \bar{\nu}$ at any given (m^2, ψ, ϕ) , holds in vacuum only.

It is amusing to notice that, in the purely hypothetical situation of equal ν and $\bar{\nu}$ fluxes at any energy E_ν , and of equal ν and $\bar{\nu}$ absorption cross sections, the symmetry T_8 would imply the same physics in atmospheric neutrino experiments in both scenarios (a) and (b).

Finally, we consider the case of $m^2 \rightarrow \infty$ or, more precisely, $m^2 \gg A$. In this limit, the oscillation probabilities in Eq. (C4) become:

$$\begin{aligned}
P_{ee} &= P_{ee}^{\text{vac}} , \\
P_{\mu\mu} &= P_{\mu\mu}^{\text{vac}} - \delta P , \\
P_{\tau\tau} &= P_{\tau\tau}^{\text{vac}} - \delta P , \\
P_{e\mu} &= P_{\mu e}^{\text{vac}} , \\
P_{e\tau} &= P_{e\tau}^{\text{vac}} , \\
P_{\mu\tau} &= P_{\tau\mu}^{\text{vac}} + \delta P ,
\end{aligned} \tag{C10}$$

where $\delta P = 4s_\phi^2 s_\psi^2 c_\psi^2 \sin^2(Ac_\phi^2 x/4E_\nu)$.

Notice that in the limit $m^2 \gg A$ not all the probabilities in Eq. (C10) tend to their vacuum value. However, in this limit all the symmetries (T_1, T_2, \dots, T_8) of the vacuum oscillation case apply. In the subcases of pure two-flavor oscillations ($\psi = 0$ or $\psi = \pi/2$ or $\phi = 0$) one has $\delta P = 0$ and Eq. (C10) simply reads $P_{\alpha\beta} = P_{\alpha\beta}^{\text{vac}}$ (averaged vacuum oscillations regime).

REFERENCES

- [1] T. Kajita, in *Physics and Astrophysics of Neutrinos*, edited by M. Fukugita and A. Suzuki (Springer-Verlag, Tokyo, 1994), p. 559; T. Stanev, in *Taup '95*, Proceedings of the 4th International Workshop on Theoretical and phenomenological Aspects of Underground Physics, Toledo, Spain, edited by A. Morales, J. Morales, and J. A. Villar [Nucl. Phys. B (Proc. Suppl.) **48**, 165 (1996)]; E. W. Beier and E. D. Frank, Phil. Trans. R. Soc. London **A346**, 63 (1994); T. K. Gaisser, F. Halzen, and T. Stanev, Phys. Rep. **258**, 173 (1995); B. C. Barish, in *Neutrino '94*, Proceedings of the 16th International Conference on Neutrino Physics and Astrophysics, Eilat, Israel, edited by A. Dar, G. Eilam, and G. Gronau [Nucl. Phys. B (Proc. Suppl.) **38**, 343 (1995)]; E. Kh. Akhmedov, in *Cosmological Dark Matter*, Proceedings of the International School on Cosmological Dark Matter, Valencia, Spain, 1993, edited by J. W. F. Valle and A. Perez (World Scientific, 1994), p. 131.
- [2] Kamiokande Collaboration, K. S. Hirata *et al.*, Phys. Lett. B **205**, 416 (1988).
- [3] Kamiokande Collaboration, K. S. Hirata *et al.*, Phys. Lett. B **280**, 146 (1992).
- [4] Kamiokande Collaboration, Y. Fukuda *et al.*, Phys. Lett. B **335**, 237 (1994).
- [5] IMB Collaboration, D. Casper *et al.*, Phys. Rev. Lett. **66**, 2561 (1991).
- [6] IMB Collaboration, R. Becker-Szendy *et al.*, Phys. Rev. D **46**, 3720 (1992).
- [7] Fréjus Collaboration, Ch. Berger *et al.*, Phys. Lett. B **227**, 489 (1989).
- [8] Fréjus Collaboration, Ch. Berger *et al.*, Phys. Lett. B **245**, 305 (1990).
- [9] NUSEX Collaboration, M. Aglietta *et al.*, Europhys. Lett. **8**, 611 (1989).
- [10] G. L. Fogli and E. Lisi, Phys. Rev. D **52**, 2775 (1995).
- [11] L. Wolfenstein, Phys. Rev. D **17**, 2369 (1978).
- [12] V. Barger, K. Whisnant, S. Pakvasa, and R. J. N. Phillips, Phys. Rev. D **22**, 2718 (1980).
- [13] Y. Totsuka, in *TAUP '95* [1], p. 547; A. Suzuki, in *Physics and Astrophysics of Neutrinos*, edited by M. Fukugita and A. Suzuki (Springer-Verlag, Tokyo, 1994), p. 414.
- [14] G. L. Fogli and E. Lisi, Institute for Advanced Study Report No. IASSNS-AST/96-31, hep-ph/9604415, to appear in Phys. Rev. D.
- [15] G. L. Fogli, E. Lisi, and G. Scioscia, Phys. Rev. D **52**, 5334 (1995).
- [16] G. L. Fogli, E. Lisi, and D. Montanino, Institute for Advanced Study Report No. IASSNS-AST/96-21, hep-ph/9605273, to appear in Phys. Rev. D.
- [17] V. Barger and K. Whisnant, Phys. Lett. B **209**, 365 (1988).
- [18] J. G. Learned, S. Pakvasa, and T. J. Weiler, Phys. Lett. B **207**, 79 (1988).
- [19] J. G. Learned, S. Pakvasa, and T. J. Weiler, Phys. Lett. B **298**, 149 (1993).
- [20] K. Hidaka, M. Honda, and S. Midorikawa, Phys. Rev. Lett. **61**, 1537 (1988).
- [21] S. Midorikawa, M. Honda, and K. Kasahara, Phys. Rev. D **44**, R3379 (1991).
- [22] A. Acker, A. B. Balantekin, and F. Loreti, Phys. Rev. D **49**, 328 (1994).
- [23] J. Pantaleone, Phys. Rev. D **49**, R2152 (1994).
- [24] S. M. Bilenky, A. Bottino, C. Giunti, and C. W. Kim, Astropart. Phys. **4**, 241 (1996).
- [25] J. J. Gomez-Cadenas and M. C. Gonzalez-Garcia, CERN Report No. CERN-TH-95-80, hep-ph/9504246, to appear in Z. Phys. C.
- [26] M. Narayan, M. V. N. Murthy, G. Rajasekaran, and S. Uma Sankar, Phys. Rev. D **53**, 2809 (1996).

- [27] O. Yasuda, Tokyo Metropolitan University Report No. TMUP-HEL-96-03, hep-ph/9602342 (unpublished).
- [28] G. L. Fogli, E. Lisi, and D. Montanino, Phys. Rev. D **49** 3626, (1994).
- [29] G. L. Fogli, E. Lisi, and D. Montanino, Astropart. Phys. **4**, 177 (1995).
- [30] E. W. Beier *et al.*, Phys. Lett. B **283**, 446 (1992).
- [31] W. Frati, T. K. Gaisser, A. K. Mann, and T. Stanev, Phys. Rev. D **48**, 1140 (1993).
- [32] Fréjus Collaboration, K. Daum *et al.*, Z. Phys. C **66**, 417 (1995).
- [33] Soudan 2 Collaboration, M. Goodman *et al.*, in *Neutrino '94* [1], p. 337.
- [34] G. Barr, T. K. Gaisser, and T. Stanev, Phys. Rev. D **39**, 3532 (1989).
- [35] T. K. Gaisser, T. Stanev, and G. Barr, Phys. Rev. D **38**, 85 (1988).
- [36] M. Honda, T. Kajita, K. Kasahara, and S. Midorikawa, Phys. Rev. D **52**, 4985 (1995).
- [37] V. Agrawal, T. K. Gaisser, P. Lipari, and T. Stanev, Phys. Rev. D **53**, 1314 (1996).
- [38] T. K. Kuo and J. Pantaleone, Phys. Lett. B **198**, 406 (1987).
- [39] Particle Data Group, L. Montanet *et al.*, Phys. Rev. D **50**, 1173 (1994).
- [40] C. Giunti, C. W. Kim, and J. D. Kim, Phys. Lett. B **352**, 357 (1995).
- [41] P. F. Harrison, D. H. Perkins, and W. G. Scott, Phys. Lett. B **349**, 137 (1995).
- [42] G. V. Dass and K. V. L. Sarma, Phys. Rev. D **30**, 80 (1984).
- [43] D. S. Ayres, B. Cortez, T. K. Gaisser, A. K. Mann, R. E. Shrock, and L. R. Sulak, Phys. Rev. D **29**, 902 (1984).
- [44] E. D. Carlson, Phys. Rev. D **34**, 1454 (1986).
- [45] G. Auriemma, M. Felcini, P. Lipari, and J. L. Stone, Phys. Rev. D **37**, 665 (1988).
- [46] Y. Minorikawa and K. Mitsui, Europhys. Lett. **11**, 607 (1990).
- [47] D. L. Anderson, *Theory of the Earth* (Blackwell, Boston, 1989).
- [48] E. Akhmedov, P. Lipari, and M. Lusignoli, Phys. Lett. B **300**, 128 (1993).
- [49] LSND Collaboration, C. Athanassopoulos *et al.*, Los Alamos National Lab. (LANL) Report No. LA-UR-96-1326, nucl-ex/9605001, submitted to Phys. Rev. C; LANL Report No. LA-UR-96-1582, nucl-ex/9605003, submitted to Phys. Rev. Lett.
- [50] C. Y. Cardall and G. M. Fuller, Phys. Rev. D **53**, 4421 (1996).
- [51] LSND Collaboration, C. Athanassopoulos *et al.*, Phys. Rev. Lett. **75**, 2650 (1995).
- [52] L. V. Volkova, Yad. Fiz. **31**, 1510 (1980) [Sov. J. Nucl. Phys. **31**, 784 (1980)].

FIGURES

FIG. 1. The neutrino mass spectrum adopted in this work. One neutrino mass eigenstate (ν_3) is assumed to be largely separated from the quasi-degenerate doublet (ν_1, ν_2) by a square mass difference $|m_3^2 - m_{1,2}^2| \simeq m^2$. The two possible scenarios (a) and (b) are physically different when the earth matter effects are included in the atmospheric ν propagation. The two square mass spectra in (a) and (b) are related by: (a) \rightarrow (b) $\iff m^2 \rightarrow -m^2$.

FIG. 2. Analysis of separate and combined atmospheric neutrino data assuming pure $\nu_\mu \leftrightarrow \nu_\tau$ oscillations ($\phi = 0$ in our framework) in the mass-mixing plane ($\tan^2 \psi, m^2$). Contours at 90% and 99% C.L. for $N_{\text{DF}} = 2$ are shown. The allowed regions are marked by stars. The last panel shows the constraints coming from the combination of established accelerator data. Notice the symmetry of all the allowed regions with respect to the axis $\psi = \pi/4$.

FIG. 3. Effects of the reduction of the neutrino flux uncertainty from the default value of $\pm 30\%$ (solid lines) to $\pm 15\%$ (dotted lines). The variations in the regions allowed at 90% C.L. by sub-GeV data (upper panel) or sub-GeV+multi-GeV data (lower panel) are very small.

FIG. 4. Separate and combined analysis of atmospheric neutrino data assuming pure $\nu_\mu \leftrightarrow \nu_e$ oscillations ($\psi = \pi/2$ in our framework), in the mass-mixing plane ($\tan^2 \phi, m^2$). Contours at 90% (solid) and 99% C.L. (dotted) for $N_{\text{DF}} = 2$ are shown. The allowed regions are marked by stars. The last panel shows the constraints coming from the combination of established accelerator and reactor data. The contours of the atmospheric ν allowed regions are not symmetric with respect to the axis $\phi = \pi/4$, due to matter oscillation effects.

FIG. 5. Bin-by-bin analysis of multi-GeV Kamiokande data in the plane of the μ and e lepton rates, normalized to their theoretical values without oscillations, μ_0 and e_0 . Solid ellipses: theoretical predictions at 1σ level ($\Delta\chi^2 = 1$). Dotted ellipses: experimental data at 1σ level. Notice how the theoretical ellipses change from the upper panel (no oscillation) to the three lower panels (best-fit cases for two-flavor and three-flavor oscillations). The fit is better in the $\nu_\mu \leftrightarrow \nu_e$ case than in the $\nu_\mu \leftrightarrow \nu_\tau$ case. The overall fit improves slightly in the 3ν oscillation case.

FIG. 6. As in Fig. 4, but excluding the earth matter effect (pure vacuum oscillations). All the contours are now symmetric with respect to the axis $\phi = \pi/4$. The regions allowed by the atmospheric neutrino data in the lower half of each panel are substantially different from those reported in Fig. 4.

FIG. 7. Three-flavor analysis of all the atmospheric neutrino data (sub-GeV and binned multi-GeV combined) in the plane $(\tan^2 \psi, \tan^2 \phi)$, for 12 different values of m^2 ranging from 1.8×10^{-1} to 3.2×10^{-4} eV². Scenario (a) of Fig. 1 is assumed. The solid (dotted) curves represent sections of the region allowed at 90% (99%) C.L. for $N_{\text{DF}} = 3$ at given m^2 . The right side of each panel corresponds asymptotically to pure $\nu_\mu \leftrightarrow \nu_e$ oscillations; the lower side to pure $\nu_\mu \leftrightarrow \nu_\tau$ oscillations. Three-flavor oscillations interpolate smoothly between these two limits.

FIG. 8. Value of $\Delta\chi^2$ for all atmospheric neutrino data (sub-GeV and multi-GeV combined) as a function of m^2 only. This figure embeds the information of Fig. 7 *projected* onto the m^2 variable. At 68% C.L. ($N_{\text{DF}} = 3$) the value of m^2 is constrained between $\sim 10^{-3}$ and $\sim 10^{-1}$ eV². For very large m^2 , the value of $\Delta\chi^2$ tends to ~ 7 (not shown) and there are no upper limits on m^2 at 95% C.L. The reduction of the ν flux error from 30% to 20% does not produce significant variations, as indicated by the thin, dotted curve.

FIG. 9. As in Fig. 7, but in the scenario (b) of Fig. 1.

FIG. 10. As in Fig. 8, but in the scenario (b) of Fig. 1.

FIG. 11. Comparison between the regions allowed at 90% C.L. ($N_{\text{DF}} = 3$) by the atmospheric neutrino data in scenario (a) (solid contours), and the corresponding regions excluded by the established accelerator and reactor neutrino oscillation searches (horizontal, dotted contours). Pure $\nu_\mu \leftrightarrow \nu_e$ atmospheric ν oscillations (right side of each panel) are excluded by accelerator and reactor data for $m^2 \gtrsim 2 \times 10^{-2}$ eV². There are no significant limits below $\sim 10^{-2}$ eV² from present accelerator and reactor searches.

FIG. 12. Kamiokande distribution of multi-GeV electrons and muons as a function of the zenith angle θ , in absence of neutrino oscillations. The agreement between the published Kamiokande simulation (solid histogram) and our calculation (dashed histogram) is very good. See Appendix A for details.

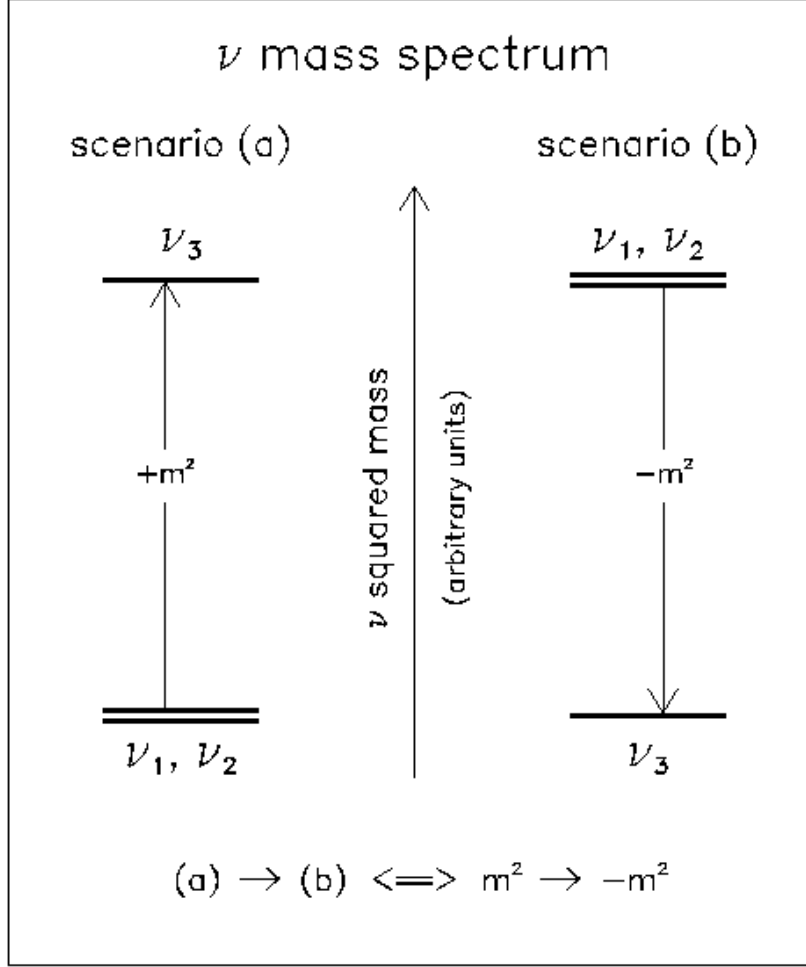


FIG. 1. The neutrino mass spectrum adopted in this work. One neutrino mass eigenstate (ν_3) is assumed to be largely separated from the quasi-degenerate doublet (ν_1, ν_2) by a square mass difference $|m_3^2 - m_{1,2}^2| \simeq m^2$. The two possible scenarios (a) and (b) are physically different when the earth matter effects are included in the atmospheric ν propagation. The two square mass spectra in (a) and (b) are related by: (a) \rightarrow (b) $\iff m^2 \rightarrow -m^2$.

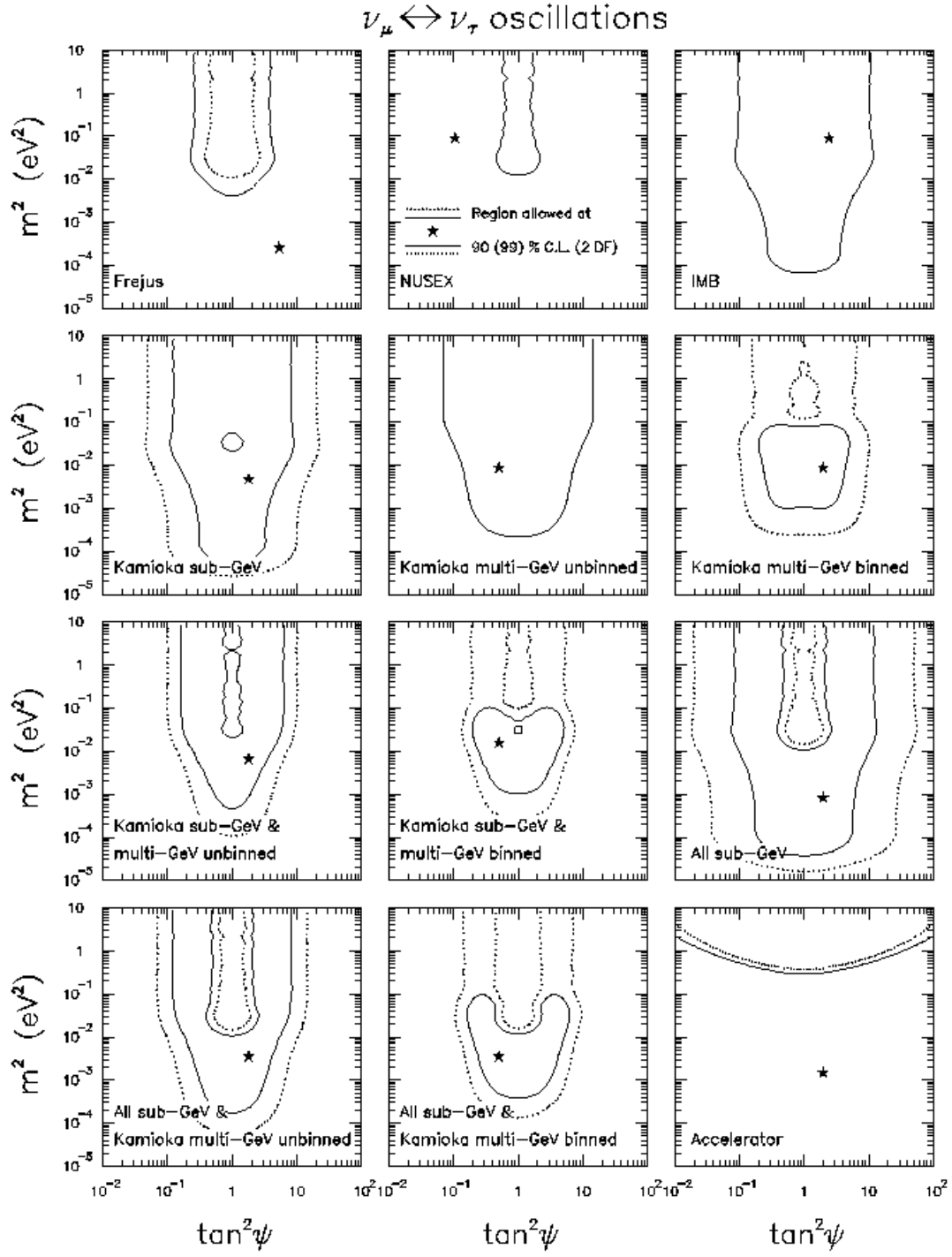


FIG. 2. Analysis of separate and combined atmospheric neutrino data assuming pure $\nu_\mu \leftrightarrow \nu_\tau$ oscillations ($\phi = 0$ in our framework) in the mass-mixing plane ($\tan^2 \psi$, m^2). Contours at 90% and 99% C.L. for $N_{\text{DF}} = 2$ are shown. The allowed regions are marked by stars. The last panel shows the constraints coming from the combination of established accelerator data. Notice the symmetry of all the allowed regions with respect to the axis $\psi = \pi/4$.

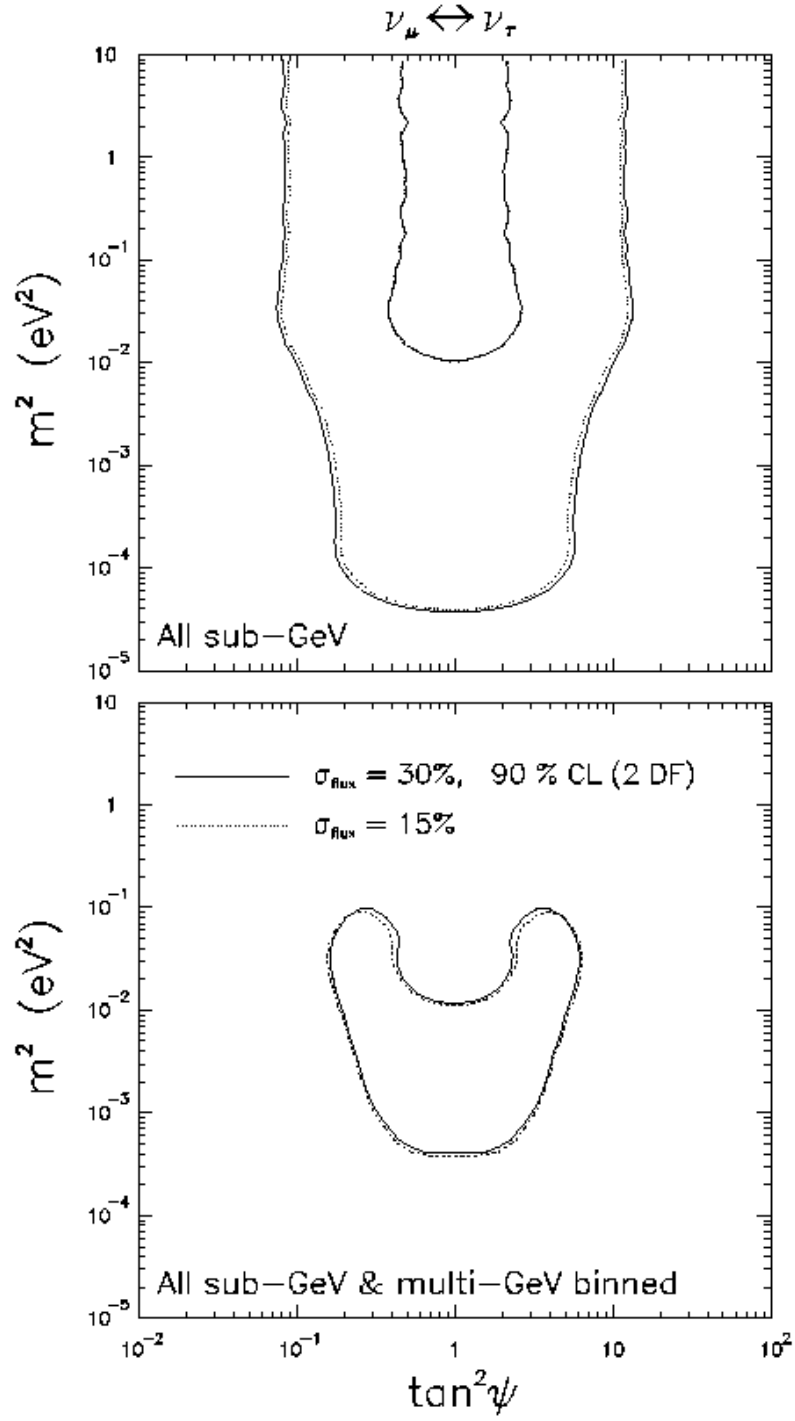


FIG. 3. Effects of the reduction of the neutrino flux uncertainty from the default value of $\pm 30\%$ (solid lines) to $\pm 15\%$ (dotted lines). The variations in the regions allowed at 90% C.L. by sub-GeV data (upper panel) or sub-GeV+multi-GeV data (lower panel) are very small.

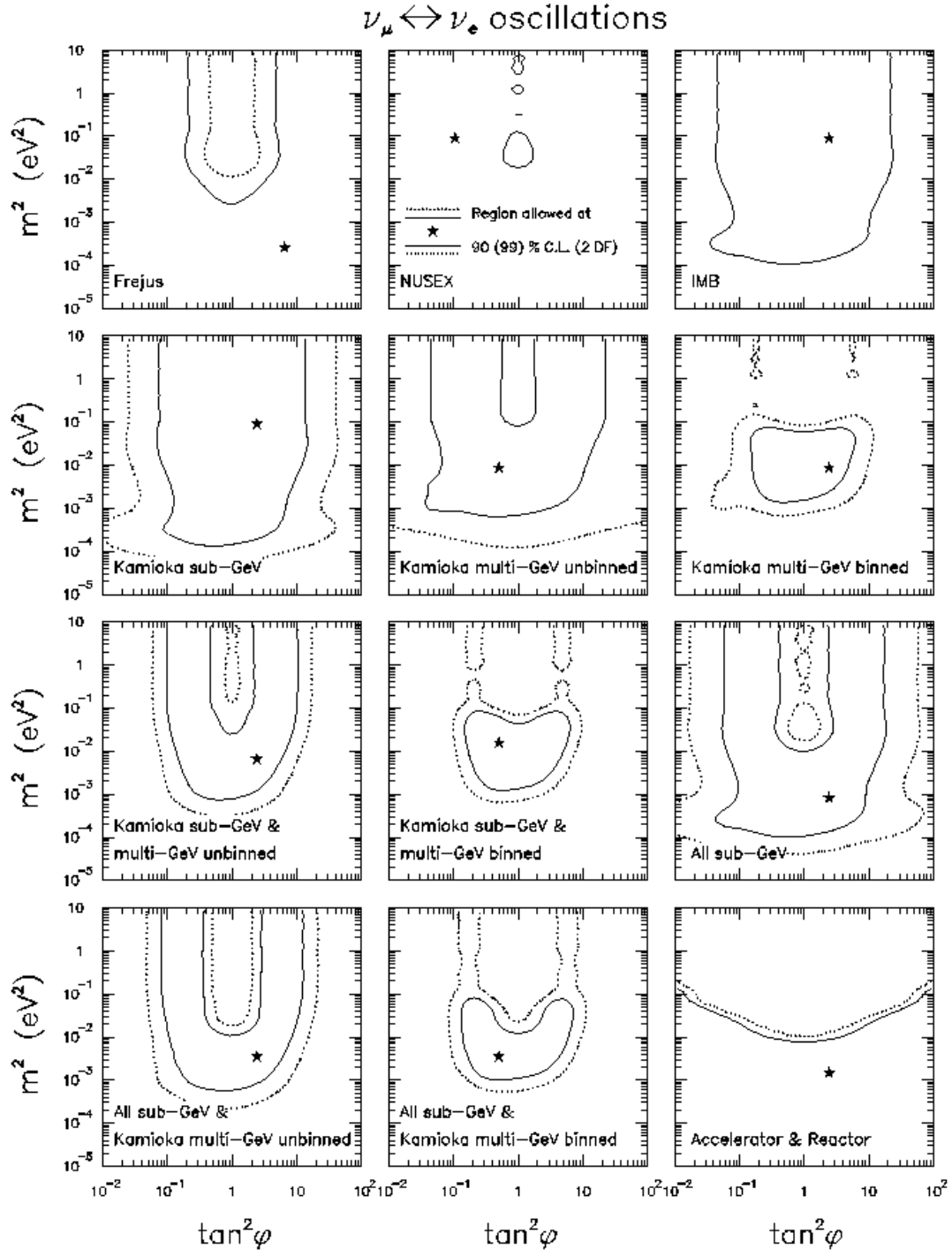


FIG. 4. Separate and combined analysis of atmospheric neutrino data assuming pure $\nu_\mu \leftrightarrow \nu_e$ oscillations ($\psi = \pi/2$ in our framework), in the mass-mixing plane ($\tan^2 \phi$, m^2). Contours at 90% (solid) and 99% C.L. (dotted) for $N_{\text{DF}} = 2$ are shown. The allowed regions are marked by stars. The last panel shows the constraints coming from the combination of established accelerator and reactor data. The contours of the atmospheric ν allowed regions are not symmetric with respect to the axis $\phi = \pi/4$, due to matter oscillation effects.

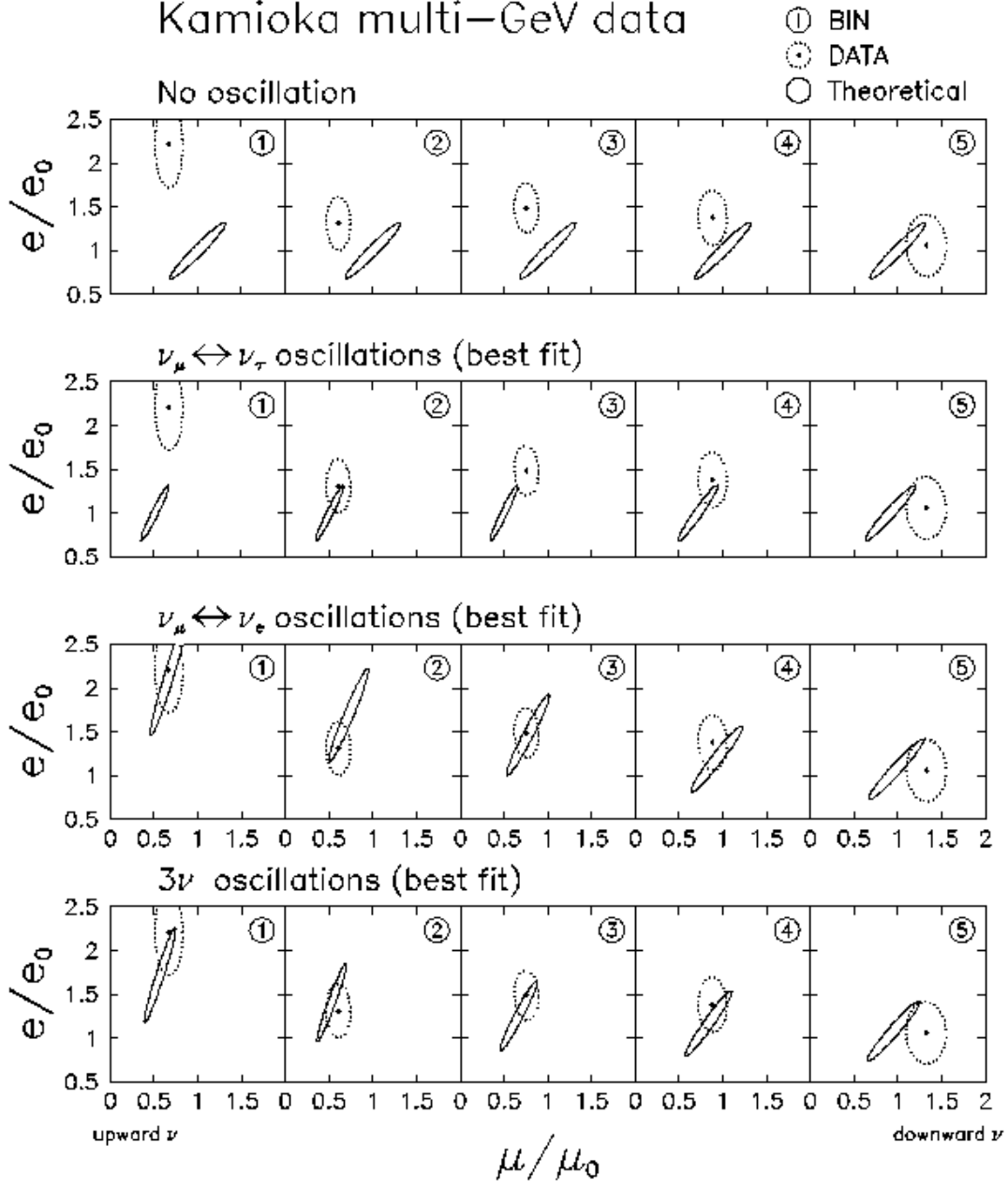


FIG. 5. Bin-by-bin analysis of multi-GeV Kamiokande data in the plane of the μ and e lepton rates, normalized to their theoretical values without oscillations, μ_0 and e_0 . Solid ellipses: theoretical predictions at 1σ level ($\Delta\chi^2 = 1$). Dotted ellipses: experimental data at 1σ level. Notice how the theoretical ellipses change from the upper panel (no oscillation) to the three lower panels (best-fit cases for two-flavor and three-flavor oscillations). The fit is better in the $\nu_\mu \leftrightarrow \nu_e$ case than in the $\nu_\mu \leftrightarrow \nu_\tau$ case. The overall fit improves slightly in the 3ν oscillation case.

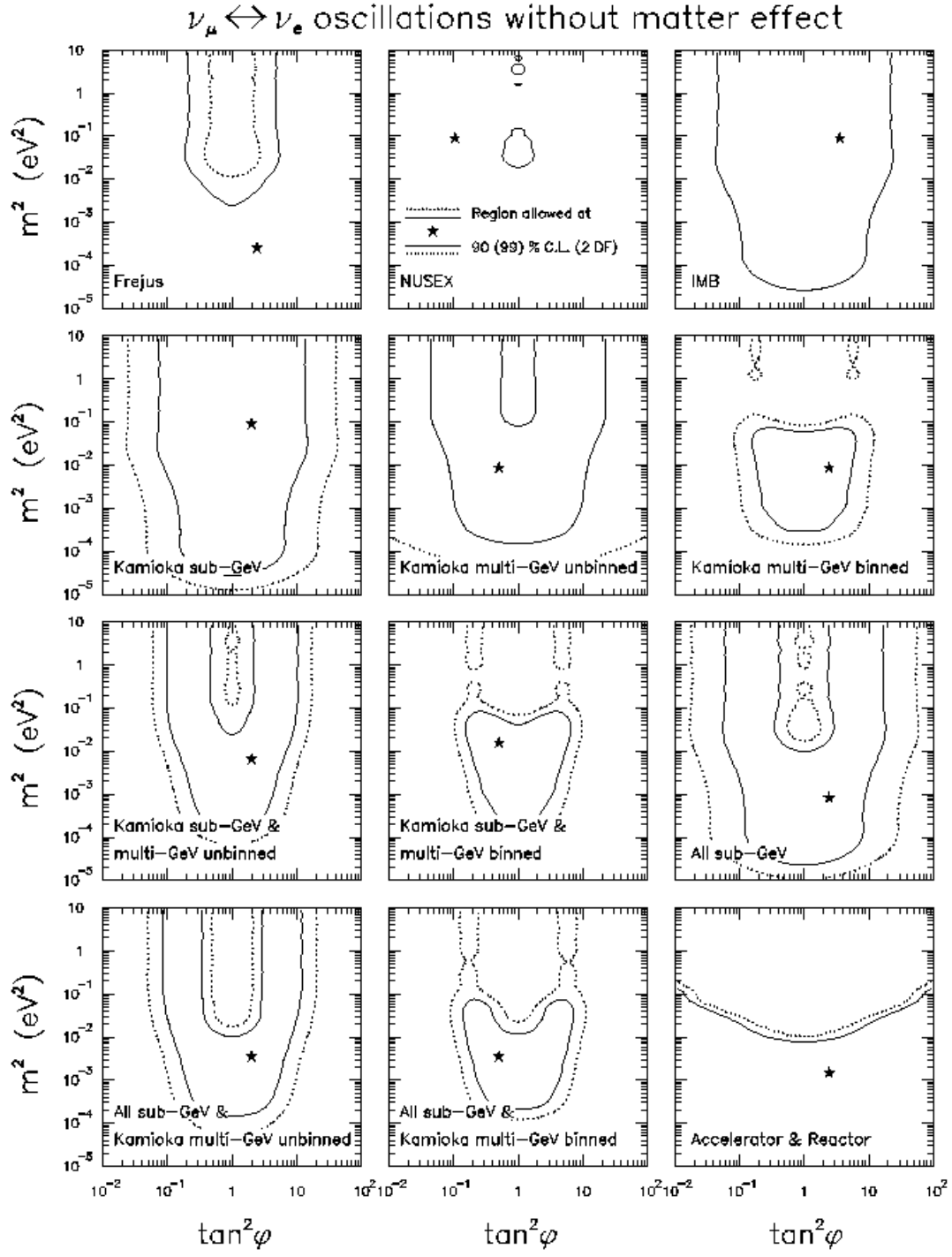


FIG. 6. As in Fig. 4, but excluding the earth matter effect (pure vacuum oscillations). All the contours are now symmetric with respect to the axis $\phi = \pi/4$. The regions allowed by the atmospheric neutrino data in the lower half of each panel are substantially different from those reported in Fig. 4.

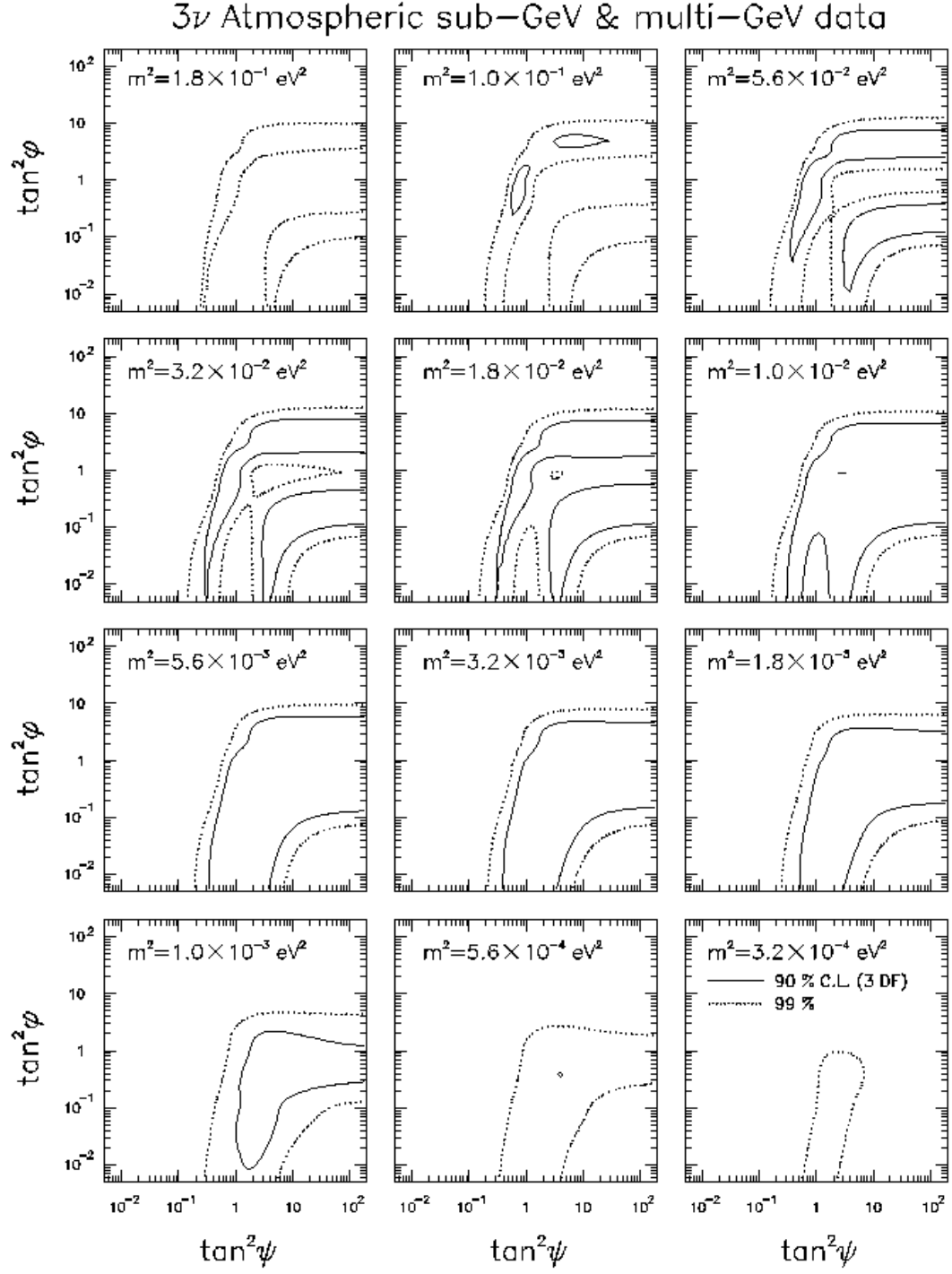


FIG. 7. Three-flavor analysis of all the atmospheric neutrino data (sub-GeV and binned multi-GeV combined) in the plane $(\tan^2\psi, \tan^2\phi)$, for 12 different values of m^2 ranging from 1.8×10^{-1} to $3.2 \times 10^{-4} \text{ eV}^2$. Scenario (a) of Fig. 1 is assumed. The solid (dotted) curves represent sections of the region allowed at 90% (99%) C.L. for $N_{\text{DF}} = 3$ at given m^2 . The right side of each panel corresponds asymptotically to pure $\nu_\mu \leftrightarrow \nu_e$ oscillations; the lower side to pure $\nu_\mu \leftrightarrow \nu_\tau$ oscillations. Three-flavor oscillations interpolate smoothly between these two limits.

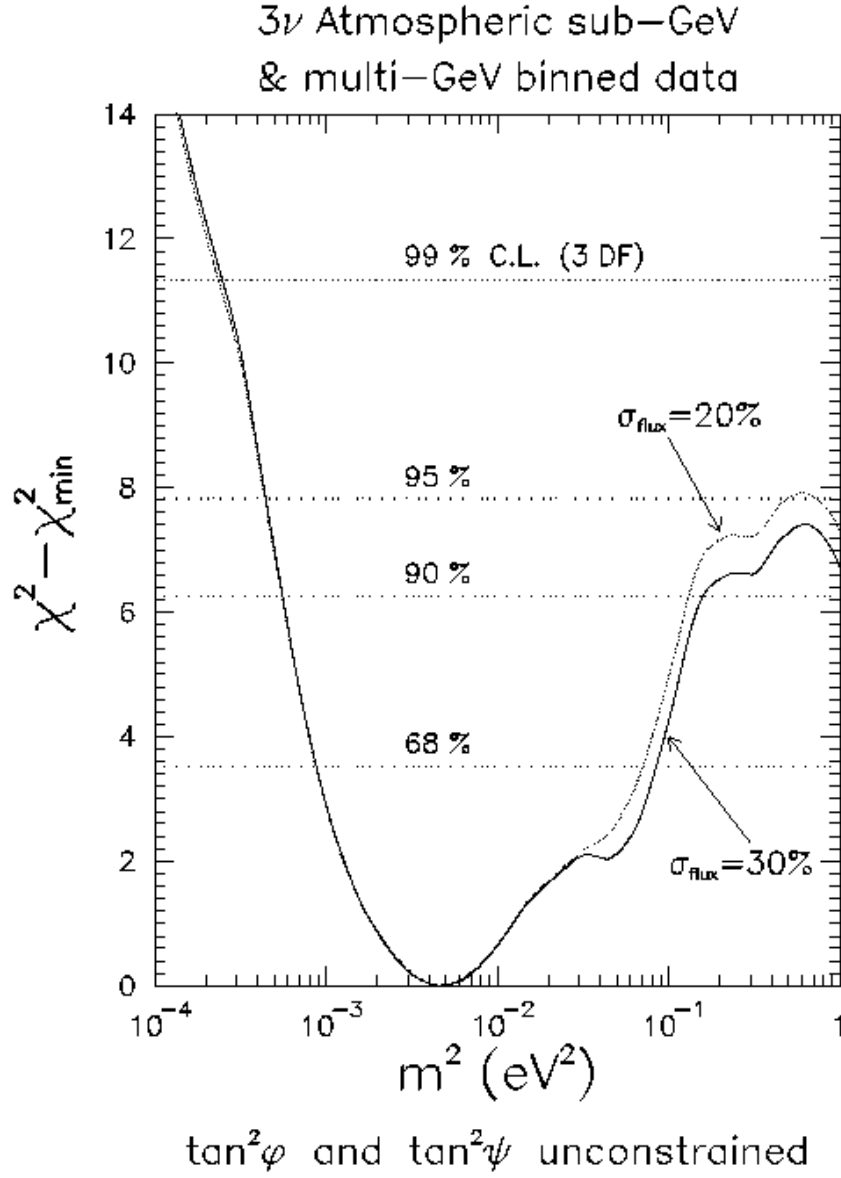


FIG. 8. Value of $\Delta\chi^2$ for all atmospheric neutrino data (sub-GeV and multi-GeV combined) as a function of m^2 only. This figure embeds the information of Fig. 7 *projected* onto the m^2 variable. At 68% C.L. ($N_{\text{DF}} = 3$) the value of m^2 is constrained between $\sim 10^{-3}$ and $\sim 10^{-1}$ eV². For very large m^2 , the value of $\Delta\chi^2$ tends to ~ 7 (not shown) and there are no upper limits on m^2 at 95% C.L. The reduction of the ν flux error from 30% to 20% does not produce significant variations, as indicated by the thin, dotted curve.

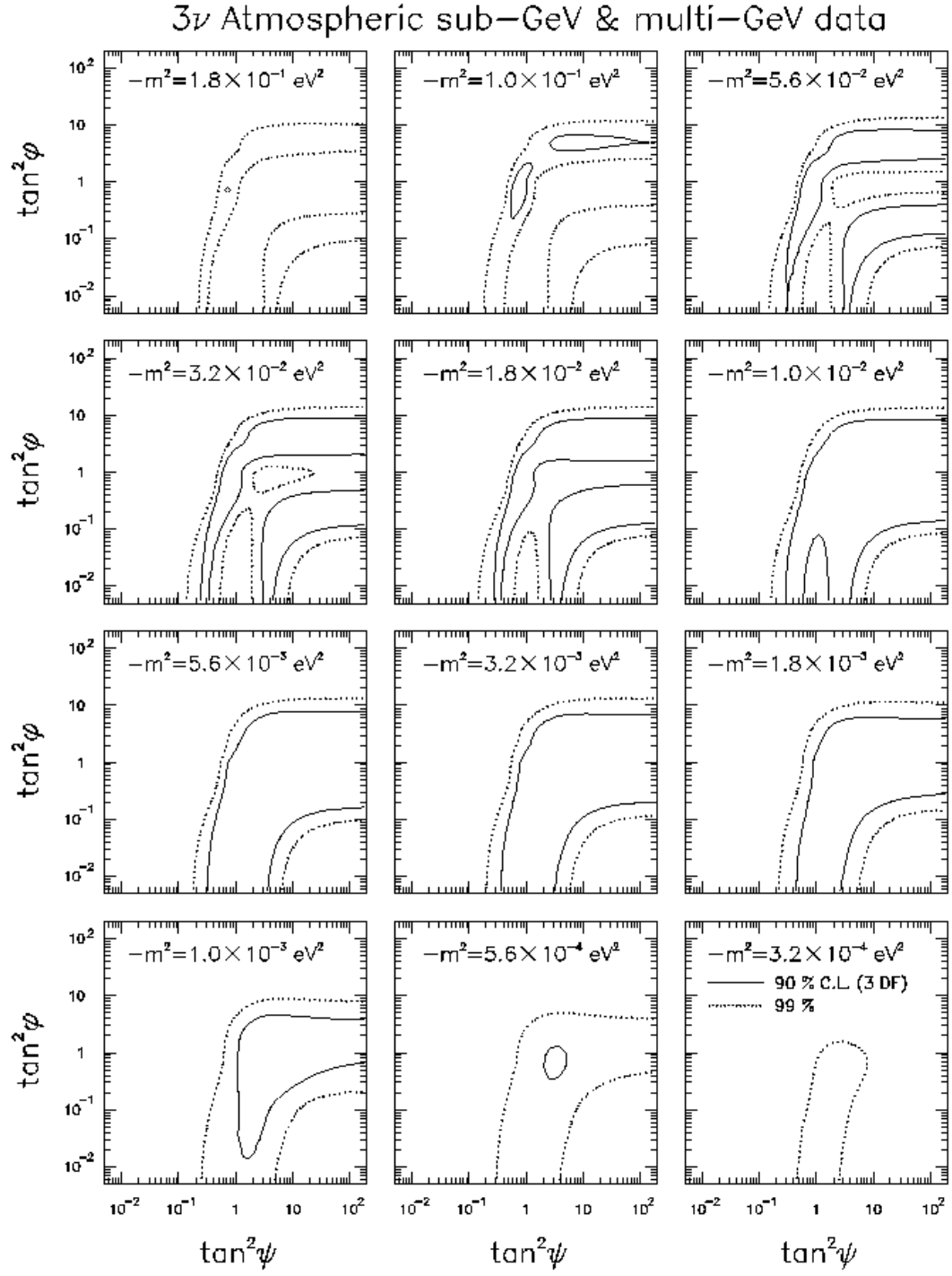


FIG. 9. As in Fig. 7, but in the scenario (b) of Fig. 1.

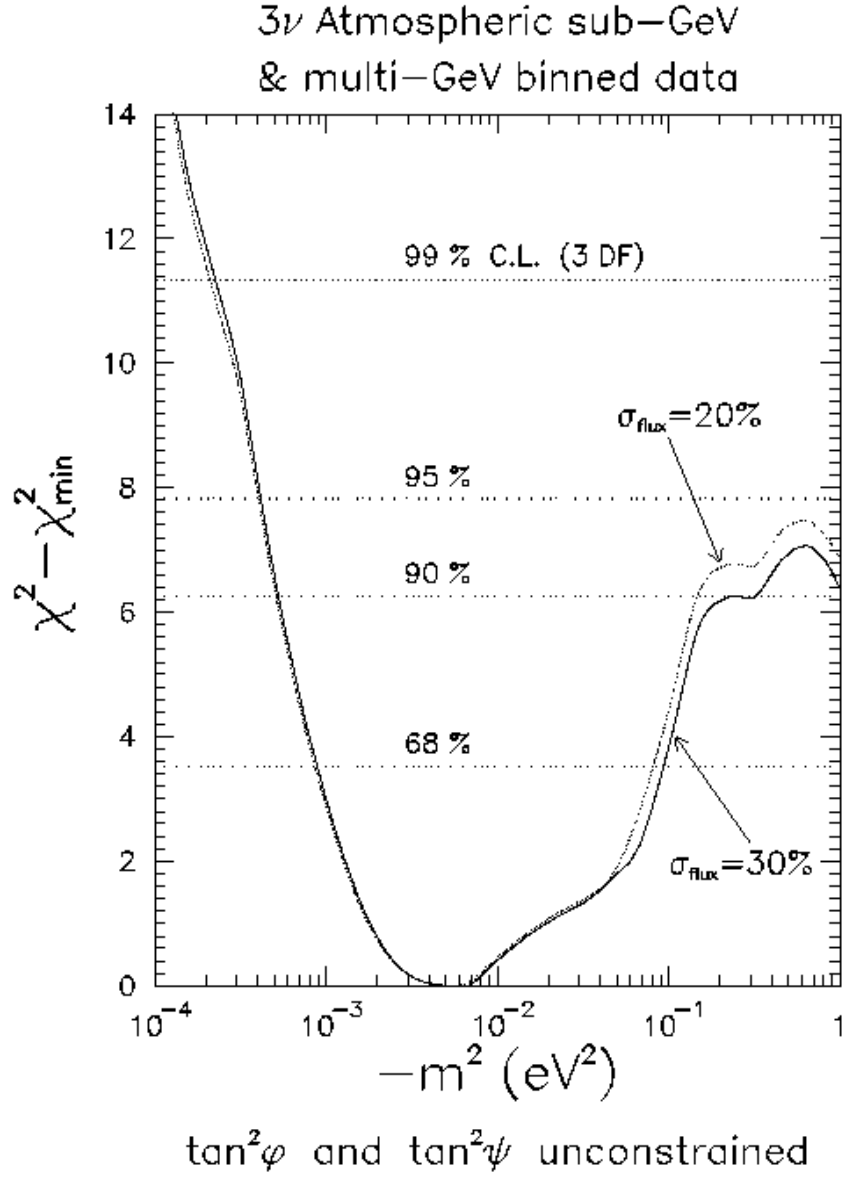


FIG. 10. As in Fig. 8, but in the scenario (b) of Fig. 1.

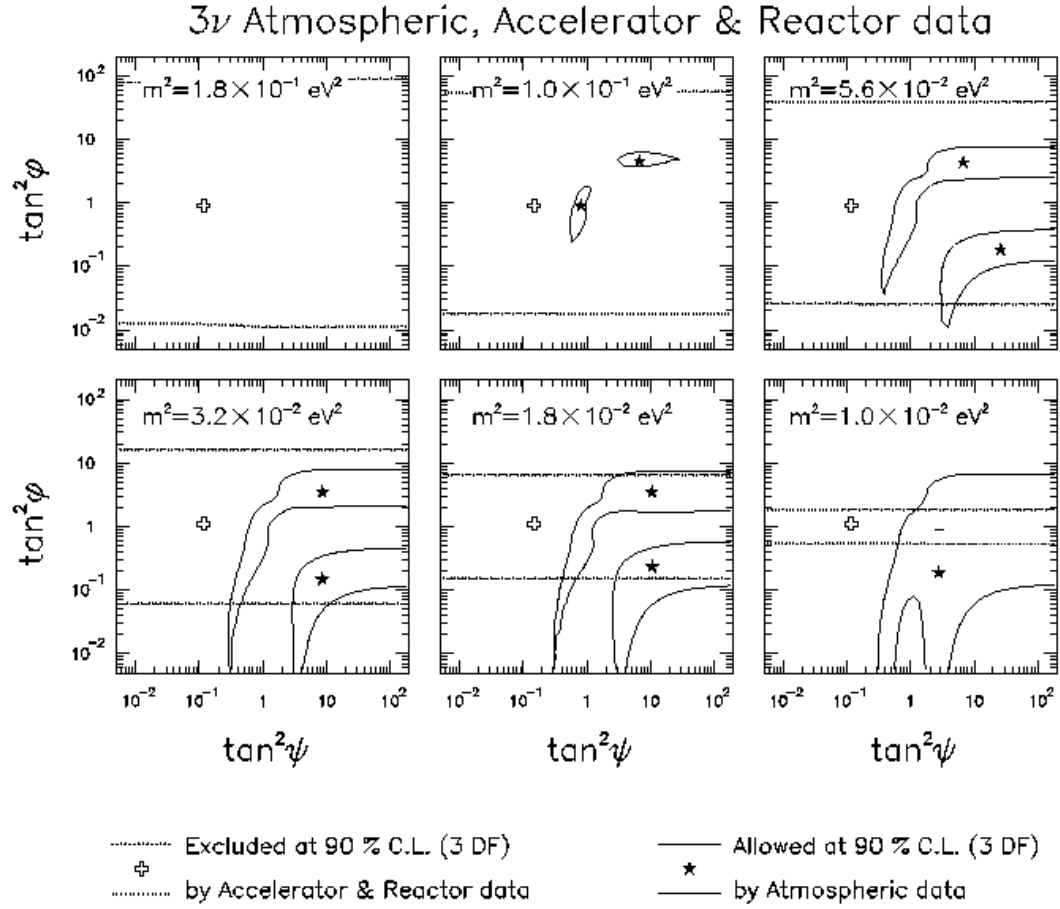


FIG. 11. Comparison between the regions allowed at 90% C.L. ($N_{\text{DF}} = 3$) by the atmospheric neutrino data in scenario (a) (solid contours), and the corresponding regions excluded by the established accelerator and reactor neutrino oscillation searches (horizontal, dotted contours). Pure $\nu_\mu \leftrightarrow \nu_e$ atmospheric ν oscillations (right side of each panel) are excluded by accelerator and reactor data for $m^2 \gtrsim 2 \times 10^{-2} \text{ eV}^2$. There are no significant limits below $\sim 10^{-2} \text{ eV}^2$ from present accelerator and reactor searches.

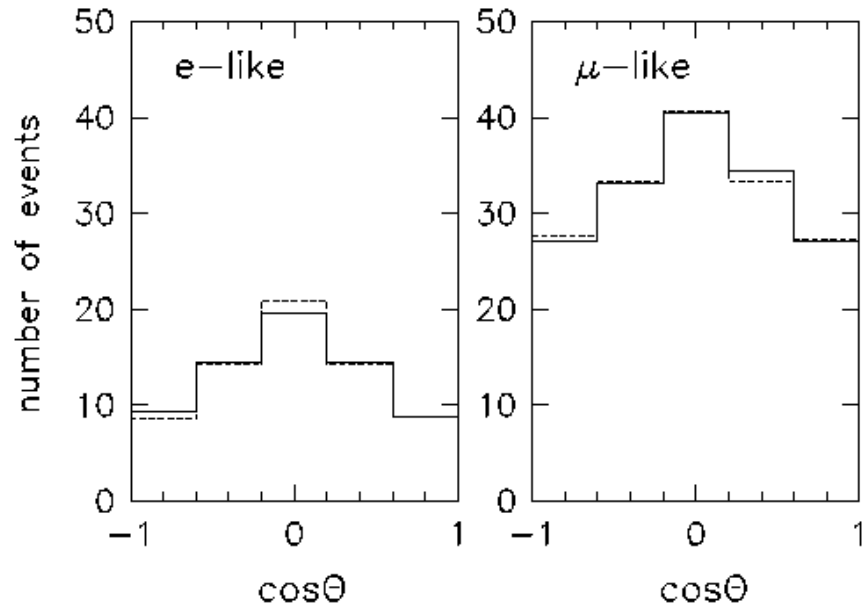


FIG. 12. Kamiokande distribution of multi-GeV electrons and muons as a function of the zenith angle θ , in absence of neutrino oscillations. The agreement between the published Kamiokande simulation (solid histogram) and our calculation (dashed histogram) is very good. See Appendix A for details.